The Taconnaz Rockfall (Mont-Blanc Massif, European Alps) of November 2018: A Complex and At-Risk Rockwall-Glacier-Torrent Morphodynamic Continuum

Ludovic Ravanel, Pierre-Allain Duvillard, Laurent Astrade, Thierry Faug, Philip Deline, Johan Berthet, Maëva Cathala, Florence Magnin, Alexandre Baratier, Xavier Bodin

applied sciences

MDPI

Article

The Taconnaz Rockfall (Mont-Blanc Massif, European Alps) of November 2018: A Complex and At-Risk Rockwall-Glacier-Torrent Morphodynamic Continuum

Ludovic Ravanel [1,*], Pierre-Allain Duvillard [2], Laurent Astrade [1], Thierry Faug [3], Philip Deline [1], Johan Berthet [4], Maëva Cathala [1], Florence Magnin [1], Alexandre Baratier [4] and Xavier Bodin [1]

1 EDYTEM, University Savoie Mont-Blanc, CNRS, 73000 Chambéry, France; laurent.astrade@univ-smb.fr (L.A.); philip.deline@univ-smb.fr (P.D.); maeva.cathala@univ-smb.fr (M.C.); florence.magnin@univ-smb.fr (F.M.); xavier.bodin@univ-smb.fr (X.B.)
2 Nāga Geophysics, Savoie Technolac, 73370 Le Bourget du Lac, France; pierre-allain.duvillard@naga-geophysics.com
3 University Grenoble Alpes, CNRS, INRAE, IRD, Grenoble INP, IGE, 38000 Grenoble, France; thierry.faug@inrae.fr
4 Styx4D, Savoie Technolac, 73370 Le Bourget du Lac, France; johan.berthet@styx4d.com (J.B.); alexandre.baratier@styx4d.com (A.B.)
* Correspondence: ludovic.ravanel@univ-smb.fr

Abstract: The glacial and torrential basin of Taconnaz (Mont-Blanc massif, France) dominates the Chamonix valley. It is one of the major paths for snow avalanches in the Alps, often triggered by serac falls from the Taconnaz glacier. On 24 November 2018, the basin's multi-risk nature was further accentuated by a new type of hazard with a rockfall triggered at *c*. 2700 m a.s.l. It travelled down over a distance of 1.85 km and stopped 165 m away from the construction site of a micro-hydroelectric power station. We studied the triggering conditions at the permafrost lower limit, the effects of the supra-glacial path on the flow patterns, and the fate of the scar and the deposit on torrential activity. By comparing a pre-event Structure from Motion model with a post-event LiDAR model, we estimated the volume of the scar to be 42,900 m^3 (±5%). A numerical model was employed to simulate the rapid runout. It revealed the complexity of the flow, attributed to the sequestration of a part of the deposit in crevasses, the incorporation of a significant volume of ice resulting in a transition from a dry granular flow to a mud-like flow, and the presence of numerous deposit zones. Subsequent monitoring of the area after the event allowed for the documentation of the scar's evolution, including a landslide, as well as the progressive degradation and evacuation of the deposit by the torrent without producing debris flow. The study of the triggering factors indicated glacial retreat as the probable main cause, assisted by the melting of ice lenses left by the permafrost disappearance. Finally, we present replicable methods for managing risks at the site following the event. This event improves the understanding of cascading processes that increasingly impact Alpine areas in the context of climate change.

Keywords: rockfall; glacier; permafrost; torrent; natural hazard; Mont-Blanc massif; numerical models

Citation: Ravanel, L.; Duvillard, P.-A.; Astrade, L.; Faug, T.; Deline, P.; Berthet, J.; Cathala, M.; Magnin, F.; Baratier, A.; Bodin, X. The Taconnaz Rockfall (Mont-Blanc Massif, European Alps) of November 2018: A Complex and At-Risk Rockwall-Glacier-Torrent Morphodynamic Continuum. *Appl. Sci.* **2023**, *13*, 9716. https://doi.org/10.3390/app13179716

Academic Editor: Adriano Ribolini

Received: 30 June 2023
Revised: 14 August 2023
Accepted: 23 August 2023
Published: 28 August 2023

1. Introduction

The study of rockfalls in Alpine regions is crucial for understanding landscape evolution and assessing a significant natural hazard. The incidence of rockfalls is on the rise in many high mountain areas [1,2], including the European Alps [3]. This trend is observed from high-elevation areas, such as cable cars and huts [4], to valley floors affected by urbanisation and transportation [5]. With reliefs that considerably increase the potential for erosion, the long, steep slopes of the high Alpine mountains can produce an acceleration and amplification of morphogenic processes [6,7]. Due to the existence of a bioclimatic gradient, these processes follow one another along the slope or even combine to affect

not only the slopes but also sometimes the valley floors [8,9], often following torrential channels. High mountain environments are thus characterised by an exacerbation of the morphogenic system, which is further reinforced by global warming [10]. It is, therefore, necessary to gain a better understanding of the processes that affect and shape high mountain slopes. Made up of steep rock faces or superficial formations, covered or not with mobile or immobile ice, the slope is multifaceted and changing. Its evolution with climate change, often conditioned by numerous other factors (e.g., topography, geological structure, lithology), can result in the destabilisation of entire slopes [11,12]. This was the case recently on Piz Cengalo (3369 m a.s.l., Bernina massif, Switzerland). The mountain has been prone to rockfalls (here defined as the detachment of a mass of rock with a volume >100 m^3 from a steep rock wall, along a series of discontinuities and its transportation downslope a variable distance) and rock avalanches (>0.1 M m^3) on several occasions, as in December 2011 when around 1.5×10^6 m^3 of rock detached [13]. Other smaller rockfalls occurred in 2012, 2016 and on 21 August 2017. Two days later, a rock avalanche with an estimated volume of 3.1×10^6 m^3 occurred, generating a series of large mudflows along the Bundäsca torrent that reached the village of Bondo [5], which was fortunately partially evacuated thanks to a warning system installed after the 2011 event. Eight climbers and hikers lost their lives. It is, therefore, important to better understand the evolution of high mountain slopes in order to better anticipate the direct and indirect risks associated with the processes that affect them.

In order to enhance our understanding and management of these emerging risks, it is essential not only to conduct statistical analyses of rockfall datasets [14,15] but also to closely examine individual events [16,17]. This approach allows us to identify triggering conditions, especially the roles of permafrost degradation and glacial retreat—both consequences of the current global warming, which is particularly accelerated in mountainous regions. Furthermore, these events offer insights into runout dynamics [12], notably the effects of supra-glacial pathways on flow patterns [18]. Lastly, comprehending the post-event evolution of scars [19] and documenting changes in deposits and induced impacts on torrential activity are crucial [20]. Surprisingly, these aspects have received relatively little research attention to date.

The Taconnaz glacier and valley in the Mont-Blanc massif (MBM, western European Alps) is a major risk site in the Alps with numerous large-scale snow avalanches over the last century [21,22], often triggered by falling seracs from a large cold-based hanging glacier [23] whose stability with global warming is a cause for concern [24]. A new, multi-risk perspective emerged with the event of 24 November 2018, when a rockfall from the 2859 m a.s.l. Taconnaz spur triggered a mixed rock/ice avalanche that travelled down 1.85 km before stopping 165 m away from the construction site of a micro-hydroelectric power station.

Approaching 5×10^4 m^3, the event is one of the largest in MBM in recent decades, along with the collapse of Brenva spur on 18 January 1997 (2×10^6 m^3) [18], Drus on 29–30 June 2005 (0.3×10^6 m^3) [25], Aiguille de Tré-la-Tête on 10–11 September 2008 (5×10^4 m^3) [26], Tournier spur on the north face of Aiguille du Midi on 29 September 2017 (4×10^4 m^3), and the Trident du Tacul on 4 October 2018 (4×10^4 m^3). The last three events were observed and documented by a network of rockfall observers in the MBM [27]. A few kilometres to the south of the MBM, the collapse of the north face of Mont Crammont on 24 December 2008 (0.5×10^6 m^3) [28] originated at 2653 m a.s.l., i.e., considerably lower than all those mentioned directly above. The little rock avalanche crossed a plateau between 2050 and 2150 m a.s.l., where it deposited the bulk of the rock mass, and a small part of the mass continued downstream, forming two branches channelled by the torrents of Arpettaz and Planey. Vertical and horizontal travel distances were 1560 and 3050 m [28].

At a time when the relationship between climate change and geomorphological processes at high elevations is becoming increasingly important (Section 2), this study looks at the conditions that triggered the little rock/ice avalanche at Taconnaz basin (Section 3)—significant in terms of volume for the north-western side of the MBM, its extent and its

proximity to issues—which occurred in November 2018 (Section 4), by analysing the triggering conditions and questioning a possible periglacial and/or paraglacial origin (Section 5). It also looks at the rock/ice avalanche runout using a numerical flow model based on depth-averaged equations and a Voellmy rheology with cohesion, the evolution of the scar and the rock/ice deposit obliterated by several snow avalanches, the dismantling of the deposit and the return of the volume to the Taconnaz torrent (Section 5), as well as the monitoring system put in place for the operational management of the risk (Section 6).

2. Morphodynamics of the High Alpine Mountains

2.1. Glacial Retreat and Associated Glaciological and Geomorphological Processes

Glaciers currently cover around 2000 km^2 in the Alps [29], compared with 4474 km^2 in 1850 [30]. This considerable loss of surface area since the end of the Little Ice Age (LIA) also affects French glaciers: they occupied 544 km^2 in the Écrins, Vanoise and Mont-Blanc massifs, compared with 264 km^2 in 2006/09, i.e., a loss of 51% [31]. Between 1900 and 2011, Alpine glaciers lost 45% of their surface area and around 50% of their volume [32]. We are witnessing a "historically unprecedented global glacier decline in the early 21st century" [33] worldwide and in the Alps in particular. This acceleration in glacier retreat is the result of a now very negative glacier mass balance in the French Alps [34] and in the Alps as a whole [30].

Glacial retreat can be accompanied by disturbances in the flow, stability, thermal regime, and drainage of glaciers and can modify the conditions of the slopes surrounding them [35]. When the front of glaciers with a temperate base (i.e., with a temperature close to the melting point) dominates a slope break following its retreat, serac avalanches are released [36,37]. The fronts of cold-based glaciers, on the other hand, are stuck to the bedrock due to the presence of permafrost at high altitudes. Ice avalanches from cold-based glaciers are the result of a mechanical break caused by an accumulation far greater than the ablation [23,38]. The current rise in air temperature is causing the temperature of these glaciers to rise. For example, it rose by 1.5 °C at a depth of 60 m (the névé/ice boundary) on the Col du Dôme (4245 m a.s.l.) in the MBM between 1994 and 2010 [39]. While the temperature of the ice beneath the hanging front of the Taconnaz glacier (3415 m a.s.l.) was still between −4 and −3 °C from a depth of 40 to 80 m in 2012, the stability of this warming glacier is under threat over the next few decades [24]. The changes in topography, thermal regime and glacial drainage associated with glacial retreat can create intra-glacial pockets of water and pro-, juxta- or supra-glacial lakes that can possibly drain rapidly [40,41].

Finally, the loss of glacier thickness is part of the paraglacial dynamic that has been underway since the end of the LIA and which has accelerated since the 1990s. The reduction or even disappearance of the mechanical support provided by the ice to a rockface or moraine, combined with changes in their thermal regime, can lead to their destabilisation at highly variable timescales, resulting in deformations, collapses or landslides [35]. For example, the 166 m post-LIA lowering in the surface of the Pilatte glacier (Écrins massif) and its acceleration since the 2000s have destabilised a volume of 400,000 m^3 in the rocky ridge on which the refuge is built, which has gradually cracked since 1985 [42]. As for moraines destabilised by glacial retreat, there are many examples of this in the MBM (e.g., Bionnassay, Tacul, Mer de Glace, Miage, Brenva) and elsewhere in the Alps, sometimes with recurrent episodes of remarkable dimensions (several thousand of m^3), as on the Belvedere glacier [35], or combined with the permafrost degradation, as on the Tortin glacier in Valais Alps [43].

2.2. Permafrost Degradation and Slope Morphodynamics

Permafrost—i.e., ground with a temperature below 0 °C during at least two consecutive years that likely contains ice—and its warming [44,45] increase slope failures in steep rock walls [46] as already observed over recent decades in the European Alps [1,3,14]. Due to the steep slopes and the possibility of cascading processes, the consequences of slope instability can be far-reaching with devastating consequences, as illustrated recently at Piz

Cengalo (see above). On 11 June 2023, a rock detachment of 1 M m^3 affected the South Peak of the Fluchthorn (Silvretta massif, Austria), rising from 3399 to 3380 m a.s.l. (data Land Tyrol). It rapidly turned into a rock avalanche, which swept down and planed the remains of the small Fluchthornferner glacier. It then carried away the water from a proglacial lake which had recently developed over a length of 250 m. Torrential floods then took over. In all, the cascading processes covered a total distance of >2.8 km, with no casualties. The development of numerous lakes in the Alps with the glacier retreat [47] heightens the risks associated with rock slope movements for the valleys [48,49].

Permafrost degradation/warming indeed affects the mechanical behaviour of the naturally fractured bedrock [35]. Rock temperature change and water percolation in cold fractured rock alter hydraulic permeability, mechanical strength, and stress fields [50–52]. The conduction of heat from the surface leads to a deepening of the active layer—the layer that thaws each warm season—triggering small-scale collapses. Beyond this active layer, however, the permafrost *s.s.* warms with the heat input over years/decades and can trigger larger-scale destabilisations faster when multilateral warming [53], even outside the summer season. Water flowing into permafrost can warm fractures at depth [54]. The mechanical strength of bedrock permafrost and the subsurface stress field change with temperature and hydraulic conditions, reducing the friction at a potential failure plane via effective stress or increasing gravitational down-slope forces [35,55].

The response of mountain permafrost to climate has also been recently addressed through the study of the mechanical processes that govern the dynamics of ice-rich debris accumulations on mountain slopes, such as rock glaciers [56]. Indeed, long-term observation of surface displacement of rock glaciers displays a spatially consistent speed-up since the 1990s [57], with an inter-annual variability of permafrost creeping rates mainly controlled by the thermal state of the ground. However, intra-annual fluctuations of velocities are also measured and point to probable additional, yet crucial, effects played by the seasonal inflow of liquid water [58]. Geomorphological consequences of these extreme changes in rheological behaviour are also reported, with destabilising rock glaciers [59].

2.3. Morphodynamic Adjustments of Proglacial Torrential Systems

Melting glaciers and permafrost degradation raise many questions about the release of volumes of sediment that could abundantly supply torrential systems, increasing their activity and the resulting risks.

A number of studies have raised fears of an increase in torrentiality linked to an increase in the supply of sediment from deglaciated areas [60–66]. They are supported by several literature reviews that report on crises in torrential activity following glacial retreats [67]. The glacial retreat phase, in particular, is described as a period when morphogenic activity is at its peak. Church and Ryder [68] proposed models for the export of materials from deglaciated areas, which show an increase in sediment supply just at the time of deglaciation. Chiarle et al. [49] show a trend towards an increase in floods and debris flows in glaciated basins, with the most significant events associated with periods of sustained rainfall and the destabilisation of moraine structures. Other work introduces sudden events, such as glacial lake outburst floods [67,69] and the possible and punctual recovery of detrital stocks by fluvial processes (sediment materials eroded) during the paraglacial sequence [70,71].

Connectivity with the slopes and the capacity for sediment transit (constitution and/or remobilisation of sediment stocks) are central to the question of the effects of climate change on torrential systems. Research has shown that these hydrosystems are, in fact, highly fragmented due to the efficiency of paraglacial storage processes. Detrital stocks are only very partially coupled to torrential channels. Knight and Harrison [67] show that the majority of sediments released from ice are stored in situ in de-iced areas. Proglacial lakes are extremely effective sediment traps. Paraglacial models of material export clearly show the transition to a new state of dynamic equilibrium. The changes are transition phases from a significant state of abundant sediment supply with spatially extensive fluvial processes

(braiding, wide active band, etc.) to a state of equilibrium with a definite sediment deficit and a channel encased in glacial and fluvio-glacial fill. Extreme events occasionally disrupt the transition, but the trend remains the same.

On the proglacial torrents on the Chamonix side of the MBM, Berthet [72] describes the sharp decline in torrent activity over the last 150 years and the consequent reduction in the potential of the torrent system to remobilise sediment sources. This does not rule out extreme phenomena that may occur (the 1920 and 1996 floods from the Mer de Glace), but which are very infrequent and have very local consequences. Glacial retreat does not imply an increase in sediment supply but, on the contrary, a decrease in input due to the inefficiency of sedimentary coupling.

3. Taconnaz, a Rather Small Glacial Basin Marked by Very High Relief Energy

The glacial and torrential basin of Taconnaz (MBM, Western European Alps, France; Figure 1) spreads on the north side of Mont Blanc (4808 m a.s.l.) from the summit of Dôme du Goûter (4304 m) to the bottom of Chamonix valley (990 m), on the left bank of the Arve torrent, over an altitude difference of 3300 m, a distance of 7 km (average slope angle: 28°), and a surface area of *c.* 7.1 km^2. The maximum width of the basin is only 1.6 km in its upper section and 1.4 km in its middle section. The Taconnaz basin is located between the communes of Chamonix and Les Houches. The MBM is essentially made up of intrusive granite in a Hercynian metamorphic series [73]. The Taconnaz area is composed of a highly fractured gneiss, with more or less mica-schist or which is migmatised, the foliation of which dips steeply towards the interior of the massif and more or less parallel to its boundaries, i.e., towards the SE. They are cut into large NE-SW panels by thicker or thinner bands of mylonite that dip roughly parallel to the SE. The 2859 m a.s.l. Taconnaz spur is located 1 km SE of the subvertical brittle Angle fault [74], partly explaining its intense fracturing. The study area is possibly permafrost-affected down to 2859 and 2642 m a.s.l. spurs according to permafrost distribution models [75,76].

The Taconnaz glacier system covers 3.7 km^2 and develops over the upstream 4.1 km (compared with ~5.2 km in the early 2000s) [77]. Upstream, the glacier is constrained to the west by Aiguille du Goûter (3863 m), to the south by Dôme du Goûter and to the east by a shallow, ice-covered interfluve separating the flows of the Taconnaz and Bossons glaciers (Figure 1). With an average slope of around 30°, the glacier's current accumulation zone is limited downstream by a 100 m-high steep rock wall, which almost divides the glacier into two parts from around 3250 m a.s.l., with a slope glacier upstream and a steep valley glacier downstream, wedged between Montagne de la Côte–Mont Corbeau (2334 m) to the east and Montagne de Taconnaz–Gros Béchar (3562 m) to the west. At this break in the slope, four-fifths of the width of the glacier produces a long hanging front, which continues even to the NE with a small hanging glacier over a length of 400 m. Finally, the accumulation zone is only directly connected to the lower part by a 175 m-wide serac fall. This situation nearly makes the downstream tongue a regenerated glacier, as it is essentially fed by the 1 km-long hanging front. The front of the valley glacier is located at an altitude of 1950 m a.s.l. (compared with 1520 m in the early 2000s) [77]. Since the last small glacier advance in the 1970s and 1980s, the glacier has lost ~1.0 km in length (average annual loss > 30 m); the front has risen by ~460 m in altitude. To the east of the basin, two glacier tongues from the Bossons glacier enter the Taconnaz basin. At the beginning of the 2000s, they were still almost confluent immediately downstream of the 2642 m spur. The upper tongue is a 500 m-long diffluence (2019) of the western vein of the Glacier des Bossons; it still joined the Taconnaz tongue in the early 2000s immediately downstream of the 2859 m spur. This same vein recently fed a small front (18,400 m^2 in the early 2000s compared with 7400 m^2 in 2019) on the same spur. The lower tongue comes from the Bossons glacier itself in the form of a 450 m-long diffluence (2019). Downstream of the various glacier fronts, the slope is still steep (~35°), with benches. 500 m lower than the current front of the valley glacier, an imposing right lateral moraine channels the flow of the torrent against the left bank for 450 m down to the water intake of a micro-hydroelectric power station in operation since

2019. The torrent then takes on a braided form for 650 m (~13°) before leading to a very imposing avalanche defence system. Mougin [78], in his book on the torrents of Savoie, states that "since it first existed, the Taconnaz torrent has always caused damage to the land along its banks", as in 1822, 1825, 1853, 1868, and 1892.

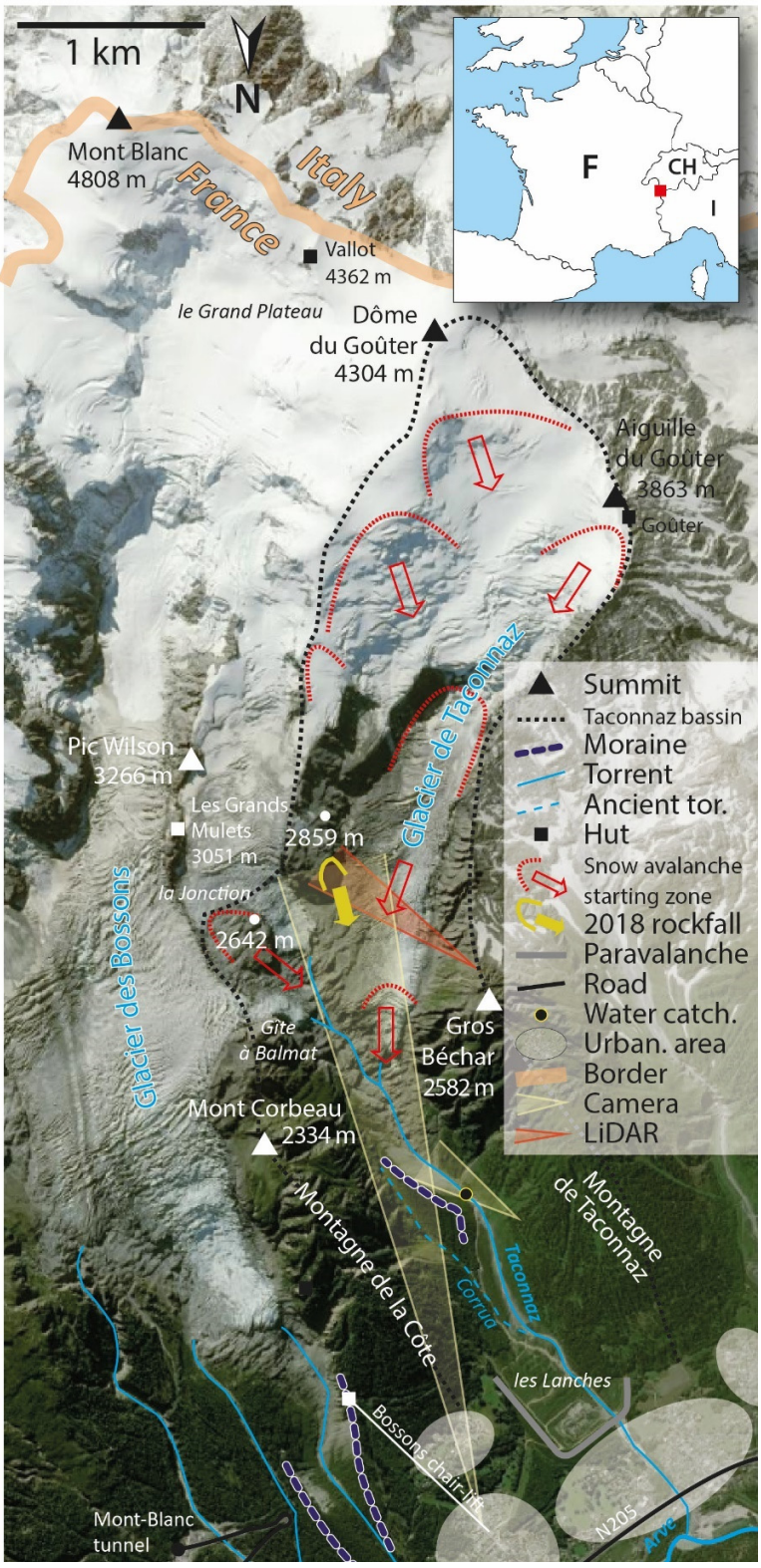

Figure 1. The glacial and torrential basin of Taconnaz (Mont-Blanc massif, France). Elevations are in m a.s.l.

During the last century, more than 70 snow avalanches were recorded on the Taconnaz path [21], including several large, dense, and mixed avalanches on many occasions reaching the inhabited areas [22]. The vastness of the starting zones (Figure 1), oriented NW-N-NE leeward of the dominant winds, represents a privileged snow deposition area and is the chief characteristic of the path. The avalanche defence system, which extends over a length of 800 m and a surface area of 0.3 km^2, is possibly the largest in the world. One has existed for many decades to protect the village downstream. In 1991, the site was equipped with a major defence system featuring reinforced concrete teeth, braking piles and dykes able to stop ~600,000 m^3 of snow and ice. Following an overflow during the avalanche crisis that affected the whole of the Alps in February 1999, this system was resized for a hundred-year event (~2 M m^3). The whole area constitutes one of the major snow avalanche paths in the Alps [22]. These avalanches are often triggered by serac falls from the hanging zone of the Taconnaz glacier [23,79]. For the past 15 years, this hanging glacier has been the subject of particular attention due to its topographic and glaciological configuration, which is dangerous for the valley [24,80].

The Taconnaz basin is long, narrow, very steep, and largely glaciarised. It is the largest avalanche couloir in Europe and as such an important object for research [22,81–83]. The Taconnaz basin is the only glaciated basin on the French side of the MBM that can produce snow and/or ice avalanches that regularly reach the valley floor.

4. The Collapse of 24 November 2018

4.1. The Failure and Deposition Zones

People living in the village of Taconnaz were woken up on 24 November 2018 at around 4:30 local time by a loud noise coming from the slope above. In the morning, a long grey-brown trail marking the passage of a small rock/ice avalanche was visible between the "2859 m spur" on the right bank of the Taconnaz glacier, now showing a large scar, and the bottom of the valley where the torrent from the glacier flows. Boulder falls and rockfalls had already been observed the previous day (e.g., S. Moatti reports two rockfalls on the glacier, stopped before the glacier front).

The 2859 m spur, located 800 m to the west of the Grands Mulets hut (3057 m), has west- to north-facing slopes. The affected area, which had an average slope angle of 50–55° before the collapse, faces NNW. The rockfall affected the entire sector between 2610 and 2760 m a.s.l., i.e., an altitude difference of 150 m between the upstream edge of the wall (~35°) and the Taconnaz glacier downstream (Figure 2). The volume mobilised consists exclusively of the gneiss found at the south-western edge of the MBM. The base of the scar is around 95 mm wide. This width decreases upstream. The collapse has excavated the rock wall, making the lower two-thirds of the scar less steep than the original slope, while the upper third has steepened significantly. The average slope angle of the scar is around 65°. The western part of the scar forms a protuberant volume whose rock is highly fractured.

Between the edge of the affected wall and the front of the deposit, the rock/ice avalanche travelled down 1.95 km, between 2760 and 1520 m a.s.l. From the top of the scar to the front of the deposit (Δh = 1240 m; mean slope: ~34°). The H/L ratio, defined as the ratio between the drop height, H, to the spreading length, L, which can be considered as the apparent coefficient of internal friction [84–86], is 0.67, a value that corresponds to a volume > 0.1×10^6 m^3. This indicates that the phenomenon is 'over-mobile' [87].

Falling onto the right lateral margin of the Taconnaz glacier, a small part of the rock mass stopped at the foot of the slope while the major part of it crossed the entire right side of the glacier's terminal tongue over a distance of 800 m, between 2610 and 2100 m a.s.l. A first sheet of supraglacial rock debris was deposited immediately at the foot of the scar (1 on Figure 3) in addition to the scree slope composed of large boulders formed at the foot of the western part of the scar (i.e., at the bottom right of the scar on Figure 2). A second sheet was deposited on the flat part of the glacier with few crevasses at around 2260 m (2).

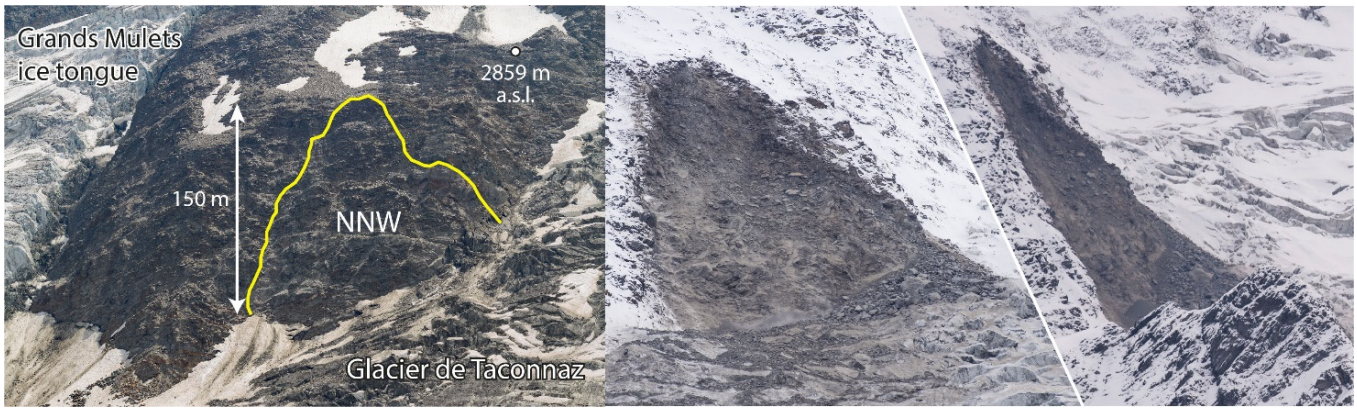

Figure 2. The scar of the rockfall of 24 November 2018. Left: the rock wall before the event (14 July 2018; ph. M. Pététin). In yellow: rockfall source. Right: the scar after the event (25 November 2018; ph. E. Courcier).

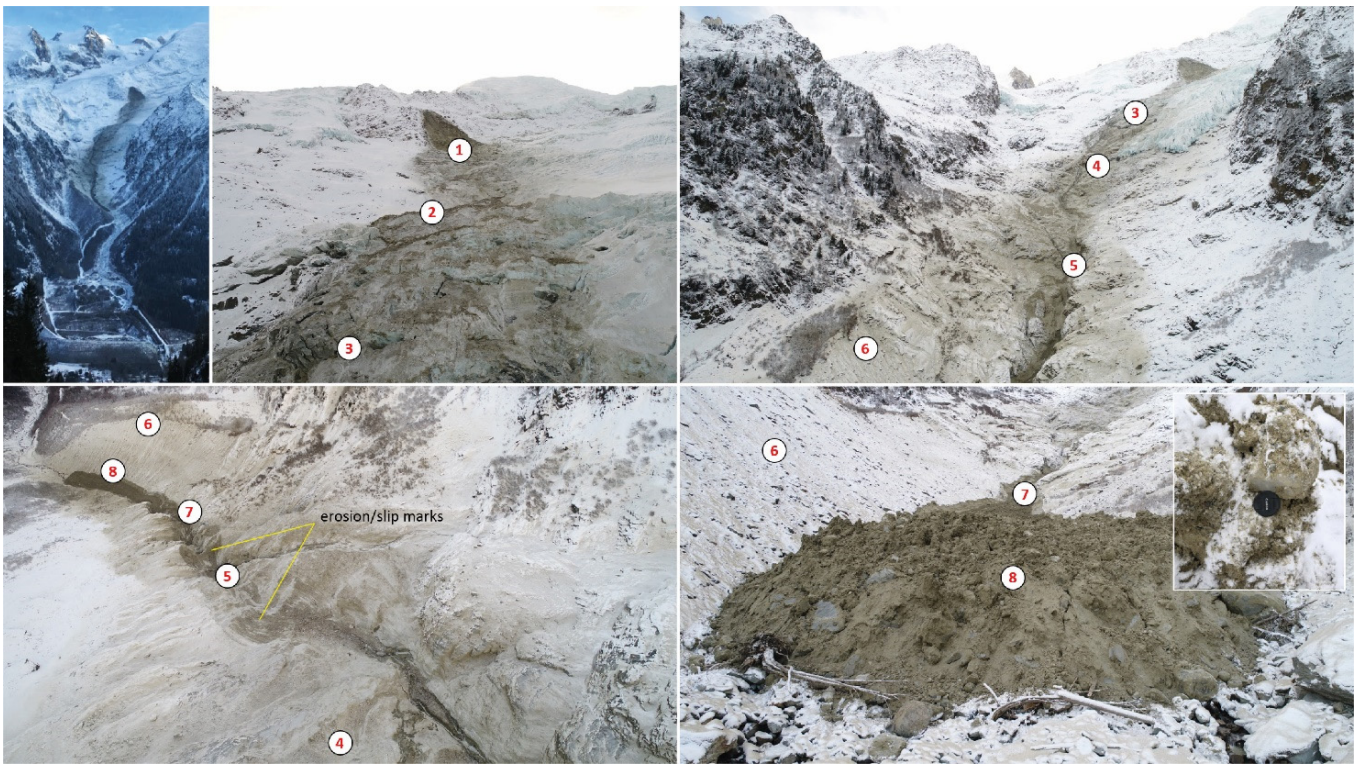

Figure 3. Path (top left: view from the Aiguilles Rouges massif; ph. C. Taillard) of the event between the scar and the front of the deposit. The deposit left in the runout zone by the dense flow is made of boulders of different sizes and shapes, with the presence of some ice blocks (inset) embedded in a cohesive matrix of fine particles. Photographs make clear the presence of an aerosol made of dust particles in suspension in the air during the flow propagation. Main images acquired by drone. Numbers: see text.

From the eastern part of the glacier front (located further upstream than the western part; 3), the rock/ice avalanche travelled down 430 m along the proglacial margin, made up of inclined rock slabs (30–35°; 4), towards the gorge drained by the Taconnaz torrent before the latter completely channelled the flow 240 m further on (5). In this steep section of the gorge, rock material of various grain sizes was deposited in relatively small quantities. On both sides of the gorge, erosion/slip marks indicated the height of the main flow (Figure 3). In addition, the aerosol of rock particles that accompanied the rock/ice avalanche deposited

dust on the surface of the snow that had fallen a few hours earlier, in some places over a width of more than 400 m (5 and 6).

The deposit becomes voluminous from an altitude of 1670 m when the slope angle of the gorge becomes much lower (7). It then develops over a length of 340 m, including around 80 m in the gorge. Downstream of the gorge, over a length of 260 m, the mass was deposited regularly in the bed of the torrent (8) at this very straight and constrained point between the slope and the right lateral moraine of the Taconnaz glacier.

The front of the deposit (Figure 3), which is steep and made up of large boulders embedded in a fine matrix (diamicton), is up to 12 m high (mean: 6.5 m). The distal part of the deposit is 36 m wide. Initially fairly constant, this width decreases towards the upstream part of the deposit. There is a significant amount of ice in the deposit. At the front, as well as on its very chaotic surface, there are many very heterometric ice blocks; while some emerge from the deposit, most are embedded in the matrix (inset in Figure 3). These ice blocks come from the erosion of the glacier's surface as the rock mass passed over it. This mobilised ice and, to a lesser extent, the incorporation of snow present on the slope at the time of the collapse, most certainly favoured the flow of the rock mass ("lubrication") and therefore increased the distance travelled. The front of the deposit, at the foot of which a few trees were pushed by the mixed flow, was located just 165 m upstream of the construction site for a micro-hydroelectric power station.

4.2. Estimation of the Volumes Mobilised

Terrestrial LiDAR (Light Detection and Ranging) and photogrammetry are two methods widely used in the study of rockfalls in high mountain areas [88–90] and elsewhere [91–95]. The volume of the collapse was reconstructed by comparing a point cloud acquired after the event (16 September 2019) by terrestrial LiDAR (Optech ILRIS-3D-ER; 2754 points per m^2) from Gros Béchar (900 m NW of the scar; Figure 1) and a point cloud before the event obtained by photogrammetry using 33 IGN (French National Institute for Geographic and Forestry Information) RGB orthophotos of 2012 (1599 points per m^2). This methodology has been widely used over the last 10 years to reconstruct post-event collapses [5,25,96].

For this study, the methodology deployed by Duvillard et al. [42] was remobilised in order to (1) generate a photogrammetric point cloud using aerial images from 2012, (2) clean the point cloud acquired by terrestrial LiDAR in 2019, (3) align the two point-clouds using the geometry of the cloud acquired by LiDAR, then (4) compare the two clouds, and (5) mesh the collapsed volume (Figure 4). Meshing, mapping, and computing rockfall volumes between 2012 and 2019 were carried out with 3DReshaper software (2016 MR1 version). The workflow described by Smith et al. [97] and applied by Guerin et al. [25] was used to generate point clouds of the rockwall using orthophotos of 2012. All the points were used for each meshing, and these were generated by a chordal deviation process with a maximum length of triangle edge of 3.5 m so as to fill the existing holes in the point clouds: the post-event cloud contains topographical masks, as it was acquired from a single position [88]. The collapse volume is 42,900 $\pm$ 2200 m^3. Uncertainty is mainly depending on the different quality of the 3D mesh.

In order to quantify the volume of the main deposit and compare it with the volume detached, a 3D model of the landslide deposit was created using photogrammetry with 437 photos taken by a DJI Phantom 4 drone on 5 December 2018. The model was geo-referenced using 11 ground control points, whose coordinates were determined through differential Global Navigation Satellite Systems. It was then compared to a 2008 LiDAR digital terrain model (from INRAE), assuming that the Taconnaz stream bed had not changed significantly between 2008 and 2018. The co-registration step involved aligning the photogrammetric model with the LiDAR model in stable areas, and the volume was then calculated only on the deposit. As the stable areas were not extensive enough, a level of detection (LoD) could not be calculated directly, so we used a LoD of 20 cm. The deposit volume was finally close to 30,000 m^3 (Figure 5). The melting of the snow and ice included in the deposit released a rockfall deposit whose volume was smaller than after the event

due to the melting of the ice. Unfortunately, we were unable to acquire a new digital terrain model at that time, which would have allowed us to accurately quantify the amount of ice in the deposit. However, we estimated the height of the remaining deposit front to be around 1.5 m. As the front of the deposit initially measured 6.5 m, the percentage of ice could be close to 75%. This means that the rock volume of the deposit would be only around 7500 m^3.

Estimating that ~8000 m^3 of rock were left at the foot of the scar, that 4000 to 5000 m^3 could have sequestered in crevasses (~1.4 km of crevasses intersected by the rockfall based on measurements on Spot6 2016 images), that the sheets of debris may possibly represent up to 10,000 or 15,000 m^3, and that the volume of the scar includes volumes that fell in 2019 (even if this is essentially a transfer of mass by slow sliding from the middle of the scar towards the downstream part of it; see Section 4.4), this result does not seem abnormal.

4.3. A Remarkable Run Out

The rockfall gave rise to a complex gravity-driven mass flow that consisted of a mixture of rock and ice, with a volume of ice that substantially increased from the scar to the runout zone because of erosion processes at stake along the path on the Taconnaz glacier. The dense flow travelled a relatively long distance, although the total volume included entrained material that was below 43,000 m^3. It formed a rather complex frontal deposit, suggesting a complex transition from an initially granular rock (rapid) flow behaviour to a more mud-like (slower) flow behaviour, which occurred due to progressive ice incorporation along the path. Moreover, the initial rock flow was accompanied by an aerosol produced by the fine dust and fine ice particles in suspension in the air.

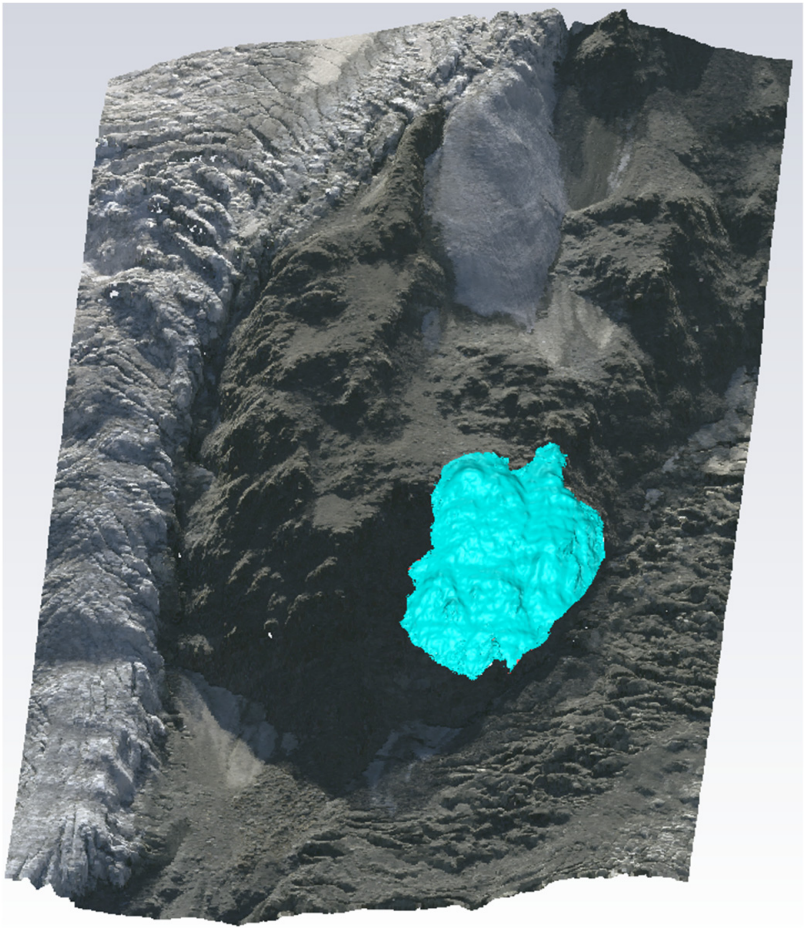

Figure 4. Three-dimensional reconstruction of the collapsed rock mass.

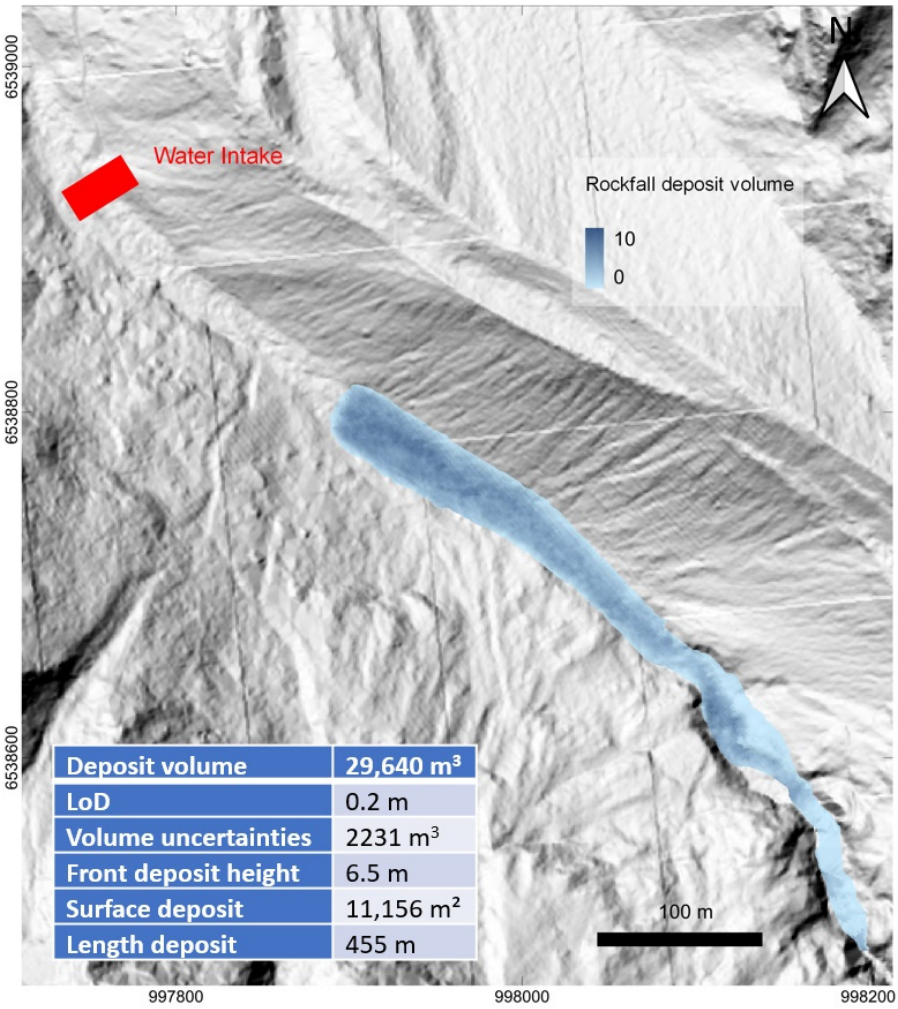

Figure 5. 2018 rockfall deposit volume estimation using the comparison of the 2008 and 2018 digital terrain models (INRAE LiDAR—photogrammetric model).

We propose a simplified back-analysis of the propagation of the rock/ice mixture, relying on a flow model based on depth-averaged equations—see details, for instance, in Naaim et al. [98]—and a Voellmy model enriched with a cohesion term for the closure rheological law. The Voellmy rheological model, initially developed for snow avalanches [99], has often been extended to case studies about rock avalanches [100], as well as ice avalanches [101–103]. For the present study case, we added a cohesive term in order to try to better account for the presence of the matrix of fine particles, as clearly detected in the deposit front (Figure 3). Preliminary simulations with the Voellmy rheological model were not conclusive at all. The closure rheological law for the basal stress τ (components τ_{zx} and τ_{zy}), which correspond to the resistive forces acting against the gravity force, is the following:

$$\tau_{zx} = [\tau_c + \mu\, \rho\, g_z\, h + \rho\, g_z(|U|^2/\xi)]\, U/(U^2 + V^2)^{1/2} \quad (1)$$

$$\tau_{zy} = [\tau_c + \mu\, \rho\, g_z\, h + \rho\, g_z(|V|^2/\xi)]\, V/(U^2 + V^2)^{1/2} \quad (2)$$

where ρ is the mean flow density, g_z is the slope-normal component of gravity acceleration, and U and V are the flow velocities in an orthogonal two-dimensional space. The rheological parameters to be considered are the dry Coulomb friction μ, the turbulent friction ξ [m·s^{-2}], and the cohesion τ_c [Pa]. Note that as we use an incompressible depth-averaged flow model framework, the cohesion τ_c is embedded in the cohesion parameter $c = \tau_c/\rho$ [m^2·s^{-2}].

The turbulent friction ξ was fixed at 1500 m·s^{-2}; this corresponds to a rather common value for rapid geophysical flows, such as rock or snow avalanches. Preliminary simulations with lower values of ξ (1000 m·s^{-2}) did not allow the initial flow to reach high velocities and then plunge into the gorge downstream of the upper part of the glacier. As we do not have any quantitative information about the flow dynamics (as the velocity at one location and/or the total duration of the flow), this parameter was then kept constant for the back-analysis because it did not influence the final runout in the torrent bed. A number of simulations were then performed by varying both the dry friction coefficient μ and the cohesion parameter c (which are considered constant all along the flow path), with the objective of finding which pair (μ, c) could give the best prediction in terms of the edges of the final deposit. For the sake of simplicity, we did not consider any erosion processes, so we avoided considering any additional parameter(s) for the back-analysis procedure. In accordance with the volume measurements, the total volume was fixed at 42,900 m^3 for the simulations, which corresponds to the total volume deposited all along the flow path from the starting point to the maximal runout point. A 1 m digital terrain model was used (Figure 6).

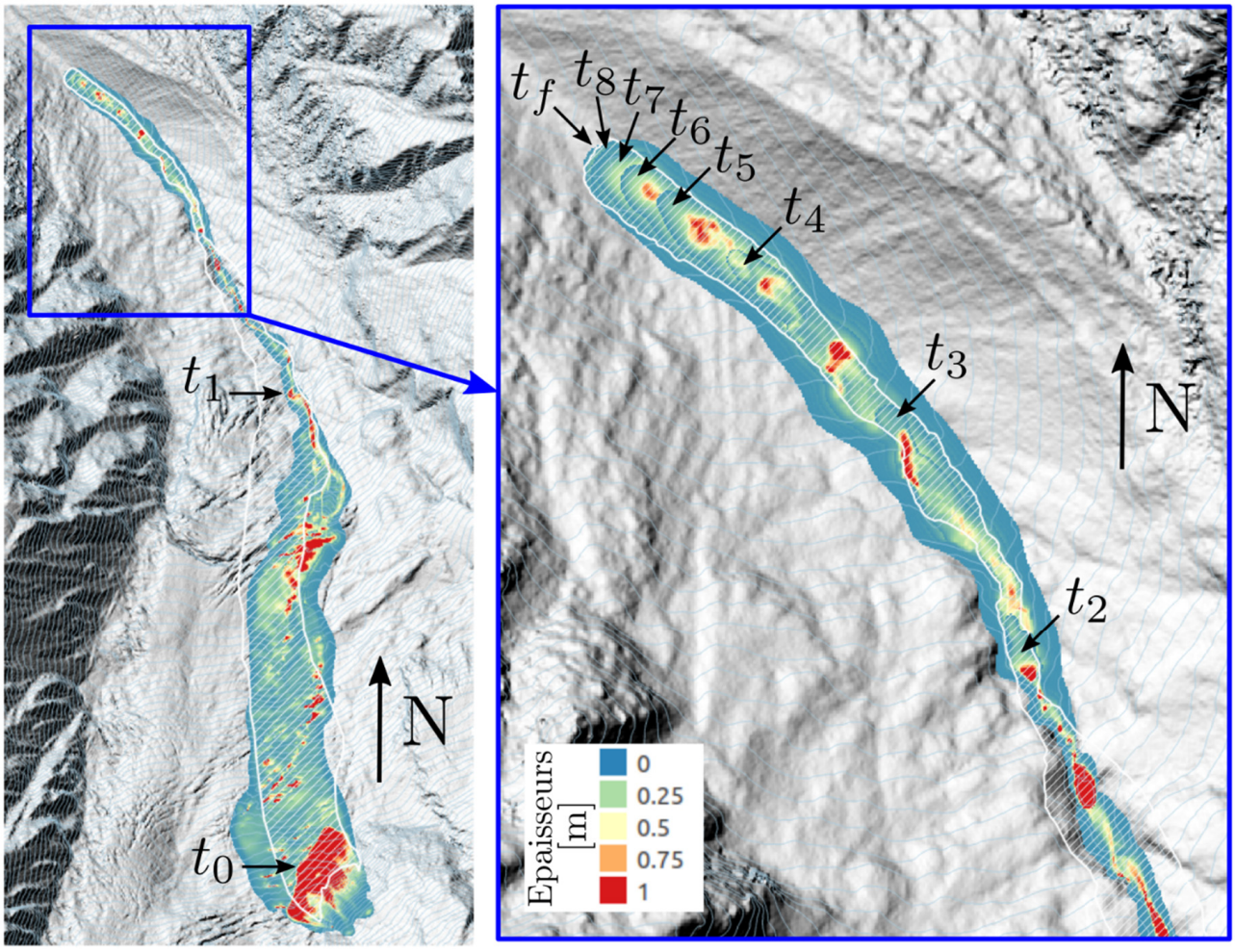

Figure 6. Left panel: snapshots showing the propagation of the simulated flow at t_0 = 6.67 s (just a few seconds after release), t_1 = 66.67 s, $t_{i+1} = t_i + t_1$ with I = {1, 2, . . ., 7} and t_f = 566.67 s (final deposit). Right panel: Zoom on the runout zone along the torrent bed. The colour levels correspond to the spatial distributions of flow thickness with a maximum threshold fixed at 1 m for each snapshot. The observed deposit left by the dense flow is depicted in hatched area in white colour for comparison.

We noted that the final runout found in the numerical simulations was quite well-constrained by choice of the pair (μ, c), in spite of a delicate interplay between the complex

topography of the terrain and the rheological behaviour (friction, cohesion) of the flow when entering the gorge. Figure 6 shows the results from the best simulation, which were obtained with $\mu = 0.17$ and $c = 0.75$ m^2·s^{-2}. Lower values of c (typically 0.5) combined with a higher value of μ gave an unrealistic total duration of the flow (which was much greater than ten minutes), and an objective arrest of the flow was very difficult to define in this case. For higher values of c (typically 1), extremely low values of μ (about 0.06) are needed to match the runout. That is the reason why the pair ($\mu = 0.17$, $c = 0.75$) was considered as the best compromise. Note that the inferred friction coefficient μ is much below the H/L ratio (Section 4.1), thus confirming the high mobility of the flow. Figure 6 shows different snapshots of the flow propagation, including the final deposit, as explained in more detail in the caption. The colour levels in the figure correspond to the flow thickness distributions. The contours of the observed deposit (see hatched area in Figure 6) are reasonably well reproduced by the depth-averaged flow model used, suggesting a single event supported by the morphology of the deposit. However, the simulations are not able to reproduce the thickness of the deposits, which appear to be systematically smaller in the simulations. While the observed deposit thickness in the runout zone is typically about a few meters, the simulated ones are about 1 m only, which is consistent with the estimated thickness of the deposit during the summer of 2019, once the ice in the deposit has melted. This significant gap may be explained by the large amount of ice involved and a stronger loss of mass during the simulations than in reality, either into the crevasses before entering the gorge or by mass trapping all along the torrent bed. We also note a greater lateral spread of the simulated flow than the observed one all along the torrent bed, which certainly contributes to making the simulated flow thinner. This shows that further model developments, in addition to a better assessment of the complex boundary conditions at stake (presence of crevasses in particular), are needed in this specific case.

These simulations should be considered as a preliminary step towards a future, much more comprehensive modelling of such a complex event with cascading effects. There are a number of uncertainties associated with the observations on the one side and with the assumptions made for the (already sophisticated) model used on the other side, which can explain the discrepancies between the observed and simulated deposits. There was a clear transition from a "dry granular" rapid rockfall (similar to a rockslide) at the starting point (fast rock fragmentation, development of an aerosol) that turned at some point into a mixture of rocks and ice with a more mud-like behaviour with much lower speed, and this was certainly caused by a huge rate of ice incorporation through erosion processes. Such a transition is difficult to capture by the model for at least two main reasons: (i) the rheological Voellmy law enriched with cohesion used in the present study did not include any additional contribution due to viscous stress which may have been a key stress contribution in the torrent bed, and (ii) erosion processes were not directly considered (the volume was kept constant during the simulation). However, such details would demand significant model developments, and calibration would still remain difficult due to additional rheological parameters needed on the one hand and the lack of observed/measured data regarding that flow transition on the other hand. An alternative approach could be to still keep the Voellmy cohesive law as a closure relation but to consider rheological parameters that would evolve along the path.

In spite of the limitations of the propagation model used here, the simulations made allow us to confirm and further highlight the great complexity of the flow certainly associated with the sequestration of a part of the deposit in crevasses, the incorporation of a substantial volume of ice along the path which results in a granular-like to mud-like transition in the flow behaviour, and numerous deposit zones formed due to the interplay between flow behaviour and complex topography.

4.4. Evolution of the Scar after the Event

The evolution of a rockfall scar is a topic that has received very little attention, including in high mountains [19,96]. Yet it is important to understand how scars evolve

and whether their evolution is a precursor to further major destabilisation. In the MBM, a network of rockfall observers has been operational since 2007 [27]. This network identified two precursor events to the rockfall of 2018: in July (~1200 m^3) and September 2016 (~300 m^3). Several events were documented by this network at the level of the 2018 scar after the collapse. In order to complete and/or verify the data, an automatic camera (Canon EOS 1000D, Tokyo, Japan; four photos per day) was installed on one of the pylons of the Bossons chairlift in order to monitor the evolution of the spur between December 2018 and December 2019. Given the long distance between the camera and the spur (3.6 km; Figure 1), additional photos were taken at each major change—recognised by the network or the automatic camera—using a Nikon D4S (Tokyo, Japan) or Fuji X-T3 (Tokyo, Japan) camera equipped with a 500 mm lens and a ×1.4 converter (Figure 7). Boulder falls, or little rockfalls (a few hundred m^3), were observed on 24 November in the early morning (e.g., F. Pallandre), in the afternoon (e.g., D. Semblanet), the following day and for two to three days (e.g., U. Asp) before a calm December. On the 26 December, regular little rockfalls signalled a reactivation of the scar, which on the 28 December led to the start of an erosive crisis with the initiation of a landslide (~8000 m^3) of the downstream bastion (Figure 7A) with associated rockfalls. This triggered a snow avalanche that stopped at the top of the avalanche protection system. On 31 December, the landslide continued briefly, triggering a rockfall (~600 m^3; Figure 7B), which in turn generated a new snow avalanche that again covered the deposit of November 2018. The landslide, with combined rockfalls, continued until mid-January 2019. On the 15th, a small rockfall occurred (~50 m^3; Figure 7C) and a larger one on the 19th (~180 m^3; Figure 7D), both within the landslide mass. Another rockfall occurred on the 5 February, still in the landslide mass, but at the western edge of the scar (~100 m^3; Figure 7E). During the second half of March, the landslide was completed, forming a large bulge at the bottom of the scar (Figure 7F), with no material exported outside the scar. No other major changes occurred in 2019 except some minor rockfalls in July (cf.: Section 6.3). Between 2020 and 2023, the sliding mass began to be gradually evacuated by the Taconnaz glacier. A new collapse occurred in May 2023 from the western edge of the scar (~700 m^3), suggesting a new reactivation of this sector.

4.5. Progressive Degradation of the Deposit and Evacuation of the Debris

The aim was to monitor the general evolution of the Taconnaz valley along the moraine between March and October 2019, at the scale of the deposit, using an automatic camera (Canon EOS 1000D; four photos per day) installed on the left bank on the slope of Montagne de Taconnaz, at an altitude of 1510 m a.s.l. (Figure 1). The photographic coverage allowed observation of the valley at an altitude of between 1400 and 2100 m. The photographs show two phases in the dynamics of the site.

The first developed over 12 days when one or more snow avalanches were identified (Figure 8), five from the two couloirs on the left bank slope (with no effect on the deposit as they reached the valley floor downstream of the front), and seven from the Taconnaz glacier, in the axis of the valley. Of these, four stopped on the deposit (forming one or more lobes), while three significant snow avalanches (on 27 March, 3 and 30 April) traversed the entire valley and continued their course beyond the hydroelectric intake. The first contributed to the snow load on the deposit, while the last, with their central depression and high lateral bulges, and in one case, the sediment load mixed with the snow, provided a spectacular illustration of the exportation of the various types of previous accumulation. These morphogenic snow avalanches certainly contributed to the reshaping of the November 2018 deposit, particularly in the upper half.

From the beginning of June, the channel is completely free of snow up to the front of the deposit, and the second dynamics become torrential (Figure 8). Flows were visible at all times, emerging under the snow and the deposit at its front. The deposit began to break up on 25 June. The time-lapse video produced from the photos shows the gradual deflating of the deposit and the snow accumulated on top of it on a continuous basis, without any sudden events and with no link to flooding, even though a torrential crisis

was anticipated due to the large volume of sediment from the rock/ice avalanche present in the channel [13,104]. However, no increase in stream dynamics downstream has been observed. From mid-July, several gaps in the snow surface were visible, and on 20 August, the valley was completely cleared of snow. The riverbed has several braided channels with a regular gradient, with no breaks or deepening of the bed due to deposit. Eight floods were observed between 20 July and the end of October. Although it is impossible to know the flow rate, quantification on the photos shows a doubling of the surface area of the active strip during these few hours (from 2.2 to 4.3 km^2 between the valley entrance and the water intake). However, there was no debris flow, the layout of the channels remained the same, and the transit of the coarse load was not accompanied by morphogenic changes. Their role in the dismantling of the deposit and the supply of debris downstream was, therefore, minimal during the observation period.

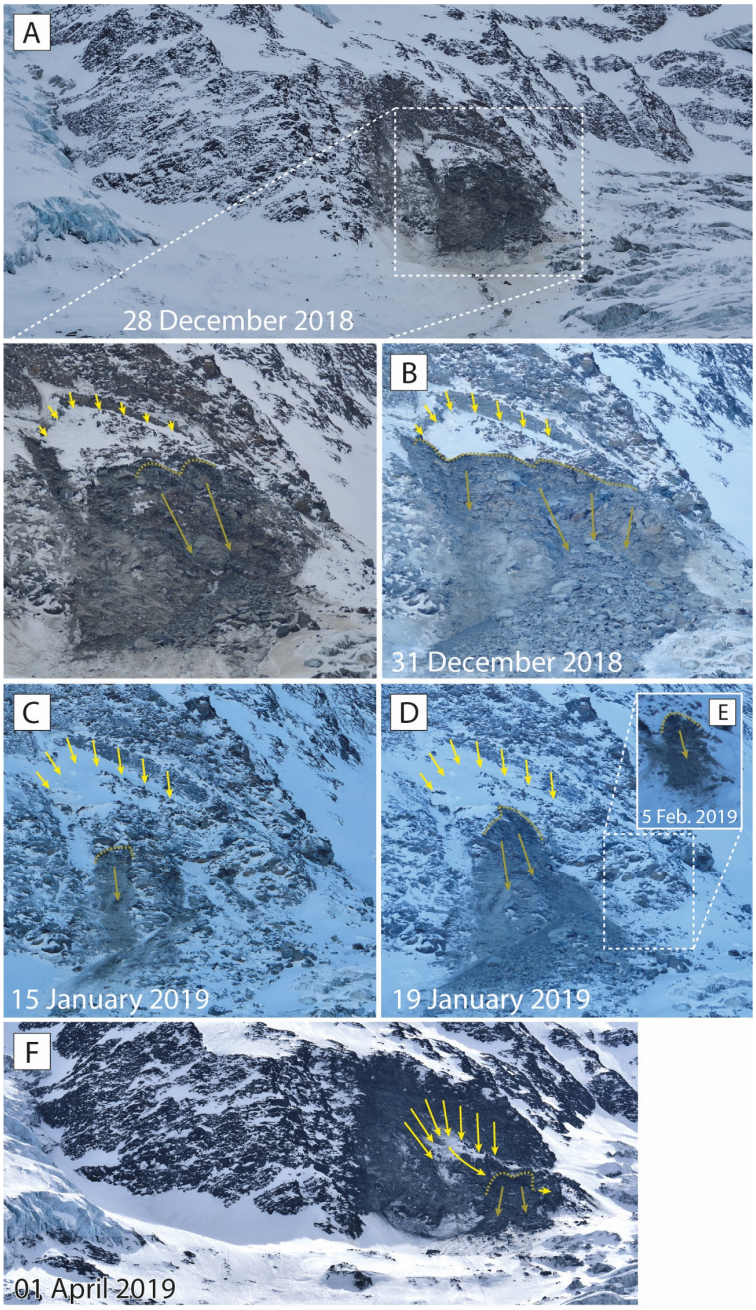

Figure 7. Main changes during the four months after the rockfall of 24 November 2018 (ph. E. Courcier). Yellow: landslide; ochre: rockfalls. Letters: see main text.

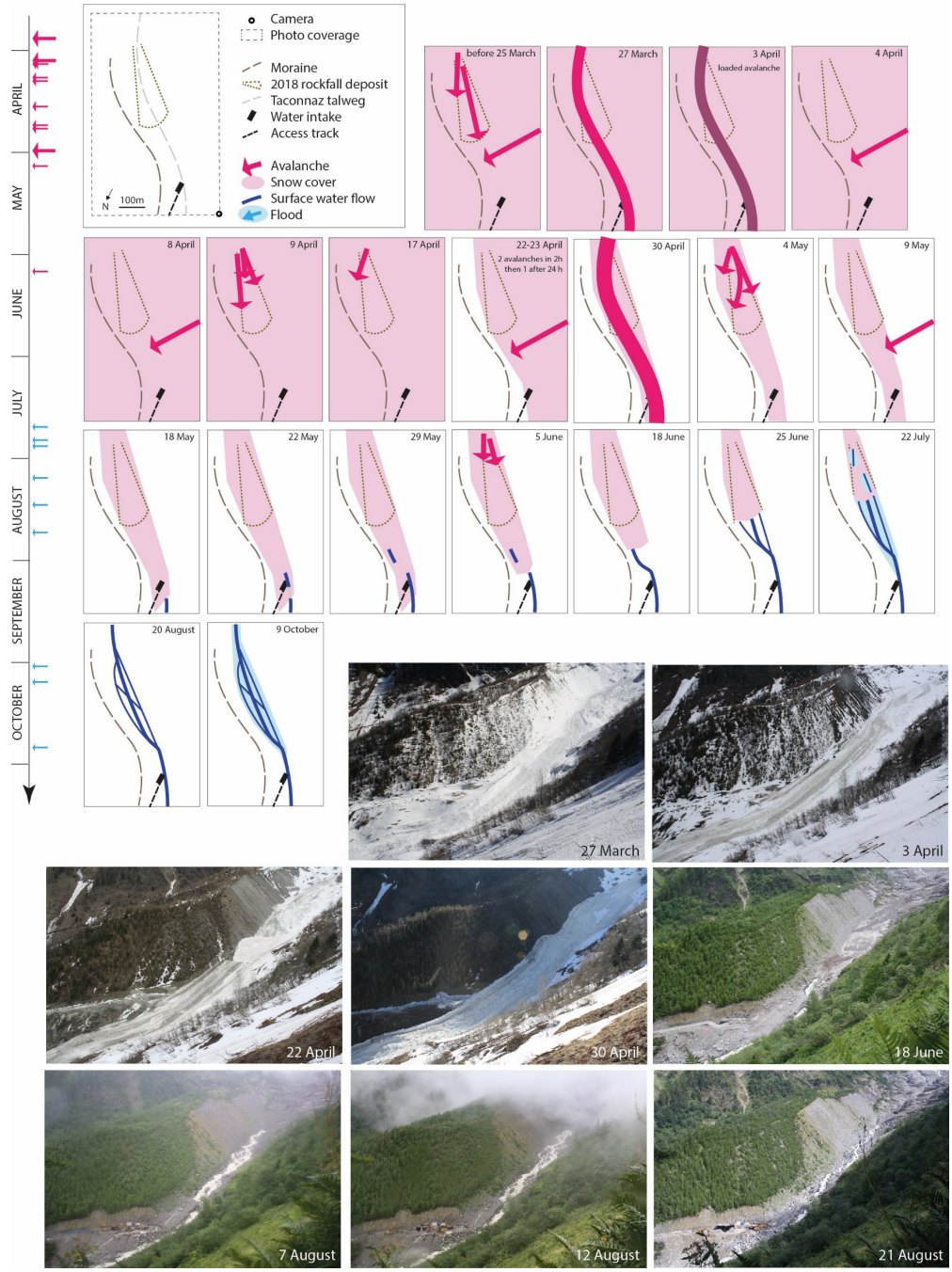

Figure 8. Evolution of the rock/ice avalanche deposit between March and October 2019. From the beginning of the monitoring period until 17 April, the entire area was snow-covered snow. Subsequently, the snow receded on the slopes, persisting only at the valley's base, where the deposit formed. Snow avalanches may continue to occur from the gorge or the left bank slope, as seen on 9 May, when an avalanche was triggered at higher altitudes.

5. A Possibly Climate-Related Event

5.1. Climate Conditions

The Taconnaz rockfall occurred after a particularly warm summer and autumn. Summer 2018 was the warmest and driest for 30 years, with a mean air temperature of 17.7 °C and only 229 mm of precipitation over the period of June–September. The period of October–November was 1 °C warmer than the average of the previous decade. This period was also the second warmest in the last 10 years. However, using air temperature from

the Chamonix weather station (1042 m a.s.l.) and an adiabatic thermal gradian of 5.5 °C every 1000 m between the weather station and the rockfall scar, the mean air temperature at the rockfall scar averaged −7.2 during the week preceding the event. 7.9 mm of rain was recorded in Chamonix—in the form of snow at the altitude of the scar and also at that of the deposit—the day before the event and 9.1 mm over the 15 days prior to the event. An episode of heavy rainfall occurred a month before the landslide, with 79.6 mm recorded in Chamonix from 26 October to 2 November. The event finally occurred during the first significant cold spell of the fall, after a particularly warm and dry summer and beginning of fall. Recent and current climatic change increases the likelihood of large slope failures in steep glacierised and permafrost terrain [1,3,46,105].

5.2. An Extremely Sensitive Permafrost Context Associated with a Hot Summer?

Warm permafrost, i.e., with temperatures close to 0 °C, is a particularly favourable condition for rockfall triggering in high mountain areas [14,106,107], due in particular to the lower mechanical strength of the ice present in the rock fractures [46,51].

The altitude of the scar, close to the lower regional permafrost limit, combined with an NNW orientation and a highly fractured rock, seemed to indicate such a periglacial context [76]. In addition, the presence of liquid water and ice in the scar (Figure 9) appeared to confirm this possibility, as did the timing of the event, which corresponded roughly to the time when temperatures are the highest at the bottom of the 10-m-deep boreholes at the Aiguille du Midi (3842 m a.s.l.) [108]. Despite this, modelling of mean annual surface temperatures at higher resolution indicates a slightly positive temperature at the scar on the one hand, indicating the possible absence of permafrost at the surface. On the other hand, the method developed by Legay et al. [107] was used to model temperatures at depth. With a porosity of 5%, the temperature on 24 November 2018 would have been +5.6 °C at a depth of 3.5 m (average depth of the scar) and +3.1 at 17 m (maximum depth of the scar). This tends to confirm that there is currently no permafrost in the rock wall. However, the warming of isolated ice-filled cracks, whose presence was confirmed by direct observation in the scar, can remain after permafrost disappearance due to the retarding effect of latent heat consumption [53] when interstitial ice melts, could have played a role in the trigger of the 2018 rockfall.

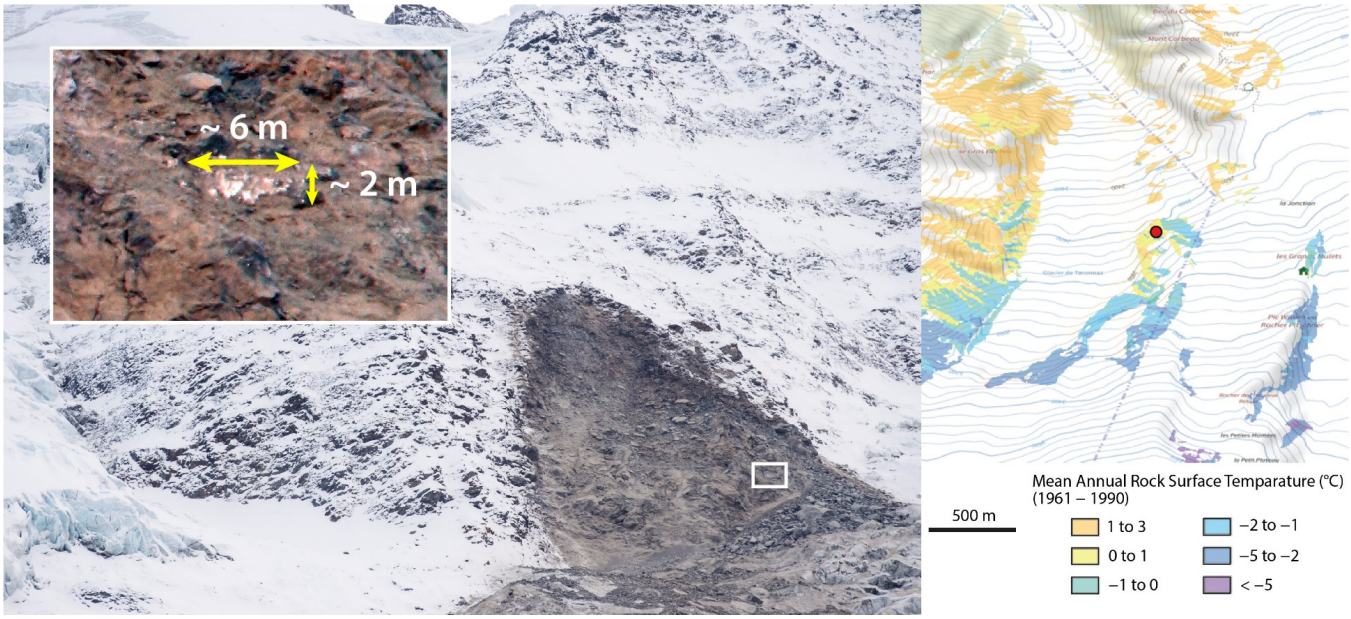

Figure 9. Massive ice present in the scar and thermal context of the rockfall (red dot).

5.3. Break-Up of the Glacial Stranglehold around the 2859 m a.s.l. Spur

Several paraglacial rock slope instabilities [109] have been the subject of detailed case studies [42,110–114]. The paraglacial concept proposed by Church and Ryder [68] describes the non-glacial processes directly conditioned by glaciation, as well as the period over which paraglacial processes are operating [70]. The response time for triggering paraglacial instability of rock slopes after the deglaciation period can be less than ten to one hundred years [70], although this remains poorly documented due to the difficulty in anticipating this process [115].

The 2859 m spur is enclosed by the Taconnaz glacier itself and by an ice tongue from the Grands Mulet ice flow from the Glacier des Bossons. Between the two, at the foot of the spur, a mass of ice seemed less mobile than both glaciers based on observations of old orthophotos (few crevasses between very crevassed glaciers). The comparison of old oblique aerial (or ground) photos with recent photos (Figure 10) suggests the possibility of a significant loss of ice thickness at the foot of the wall affected by the collapse in 2018. The comparison of 1967–2012 3D reconstructions from IGN orthophotos (Figure 10) confirms this, with an average thickness loss of >15 m. This glacial shrinkage could have caused changes in the stress regime of the rock slope, which may have played a role in the rock mass movement [60,63,116,117]. Like in the Taconnaz case, this geomorphological process can be the source of indirect threats to infrastructure through cascading processes [13].

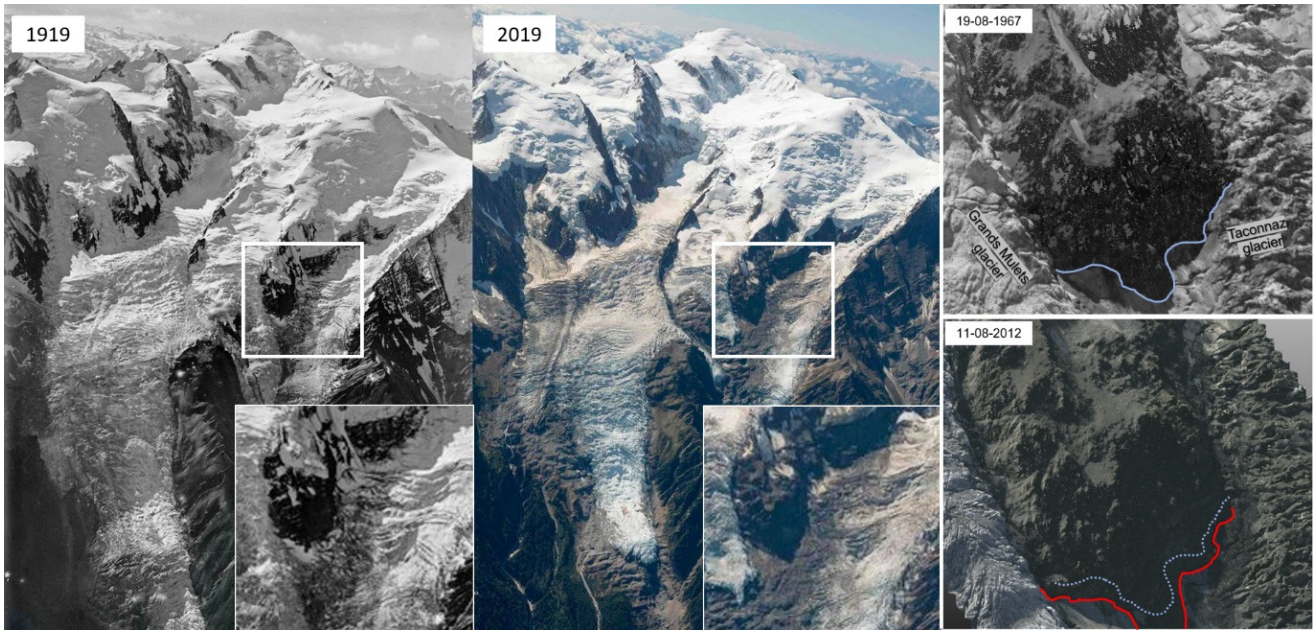

Figure 10. (**Left**) comparison of oblique aerial photographs (ETH-Bibliothek Zürich/Dr K. Baxter, University of Dundee). (**Right**) comparison of 3D reconstructions from IGN orthophotos.

6. Afterward Geomorphological Approach to Operational Risk Management

The 2018 events stopped approximately 165 m upstream of the water intake of a hydropower project. Since the summer of 2019, the awareness of the risks after the 2018 rockfall has been high (very high-energy watershed, intense, polygenic processes, and cascading risks), and an operational monitoring system has been put in place to anticipate future collapses and debris flows in order to reduce worker exposure during the construction and maintenance phases. Hydropower projects are indeed vulnerable to global warming-induced melting and thawing of the cryosphere [67,118].

6.1. An Exposed Site for the Construction of a Micro-Hydro Power Plant

The water intake is located at 1471 m a.s.l. at the base of the right lateral moraine (Figure 1). The collected water is then conveyed by a 1.7 km long penstock to the pro-

duction plant located 1041 m downstream of the avalanche defence system. The water is collected at the bottom of the torrent with a grid to filter the coarse solid load. The water flow is then driven to a grit chamber in order to reduce the solid load as much as possible before transferring it into the penstock. The very high solid load of the torrent requires regular interventions by operators in order to empty the grit chamber manually or with a mechanical shovel the blocks on the grid. These operators are exposed to three types of hazard (apart from snow avalanches which occur outside operations): (1) glacial instabilities of the three tongues, such as serac falls or front destabilisations (including hanging glacier) [38], (2) cascading process from rockfalls triggering debris flows [119], (3) rupture of an intra-glacial water pocket leading to rapid debris flows [120].

6.2. Design of the Hazard Monitoring

Hazard monitoring and assessment are seasonally and daily performed. Since June 2020, a seasonal assessment has been conducted to measure the evolution of the volume of the tongue coming from the Bossons glacier. A specific survey is carried out using aerial photogrammetry by helicopter, followed by an ice avalanche simulation using RaMMS (Rapid Mass Movement Simulation) software with different volume scenarios [101]. The compilation of the 3D models allows a quantitative assessment of the changes in volume and geometry of the ice tongue.

Daily monitoring of the deformation and speed of all the glacier tongues and rock spurs with a high-definition time-lapse camera has been carried out since June 2019. The camera is installed in the avalanche defence system from May to November. It is a self-powered system consisting of a 45 Mp reflex camera, a transmission modem and a solar panel and battery. The images are then made available on an online viewer and sorted according to cloud cover. These images are also aligned by coregistration, and the velocity fields or deformation are calculated automatically before analysis and expertise. This information is used to produce a weekly or daily ice/rock instabilities bulletin to provide information on the evolution of hazards in relation to weather conditions. In the Alps, several glaciers are monitored by time-lapse cameras and automatic analysis of velocities and deformations for natural hazard prediction and evaluation, such as the Weissmies glacier in Switzerland [121], Argentière glacier on the French side of the MBM [122], and Planpincieux glacier [37] or Grandes Jorasses (Whymper glacier) on the Italian side [123].

During each phase of the work or intervention, a watchman is stationed in the field to keep an eye on the whole area and provide any necessary alerts. The operator sits in a safe and clear viewpoint and away from the noise of the work or the torrent. In case of slope movement, the operator activates an alarm that indicates an immediate evacuation of the hydroelectric water intake. In case of bad weather conditions and poor visibility, an alert is given for every suspicious noise by the operator. Two main hydrometeorological risk situations have been identified. (1) Heatwaves. The frequency of instabilities increases with temperature. The inflow of water into the glacial system from the melting of ice and snow also modifies the pressure conditions in the sub-glacial channels [124]. This increases the risk of ice destabilisations, as the flow rates are much higher. In addition, rockfalls are more frequent during heatwaves [14]. (2) Rainstorms. Although there is no specific study linking glacier instabilities and precipitation, it has been assumed that the inflow of water into the glacial system increases the risk for the same reasons as during heatwaves. The risk of flooding is obviously high. A significant number of GLOFs (glacial lake outburst floods) following heavy precipitation have also been reported [125,126]. In case of such a situation, the level of vigilance is raised. For heat episodes, especially when they are repeated during the summer, a high level of vigilance is maintained throughout the season since the increase in the number of rockfall events lasts several weeks [127] or months [107].

6.3. Sequence of Geomorphological Events and Their Management

From 6 July 2019, the west margin of the 2018 rockfall scar was reactivated, with almost daily visible boulder falls and little rockfalls observed on timelapse camera footage.

A helicopter flight on 23 July showed that the rock compartment potentially affected by the reactivation had a much smaller volume than the one that caused the November 2018 rockfall. If the whole compartment had collapsed, it would have, therefore, been unlikely for the deposit to reach the work area. Therefore, the risk was deemed acceptable for the continuation of the work. The level of activity of the scar then decreased until the following winter and has remained zero since. This event resulted in improved diagnostics. While visual observations provided operational insights, it was necessary to adopt a strategy for quantifying events, including glacial, gravitational, and torrential ones.

On 1 October 2019, a flood occurred from the tongue of the Taconnaz glacier when the workers had just arrived at the level of the water intake for cleaning work. A retrospective analysis of the timelapse images made it possible to retrace the triggering. A migration of the location of the glacial outfall of a few tens of meters on the right bank took place between 30 September and 3 October 2019. In view of the high flows observed, it is likely that the flood is a consequence of the rupture of an intra-glacial water pocket. However, no meteorological or deformation event had been observed during the previous weeks. The reason for the change of outlet water is therefore unknown. The decrease in the speed of the ice tongues at the end of the summer can be explained by the gradual decrease in the circulation of subglacial water. The thinning of the ice tongue from the Bossons glacier after its advance of nearly 100 m between June 2020 and June 2022 is also visible.

Finally, during the summers of 2020, 2021, and 2022, a weekly risk assessment report was sent to *Voltalia* in charge of the micro-hydropower station, in order to adapt and secure its personnel during interventions at the water intake. Given that the cryosphere in the Taconnaz basin is still widely present, it is likely that this monitoring will continue over the long term.

7. Conclusions

The Taconnaz rockfall of 2018 mobilised 43,000 m^3, making it one of the largest in MBM in recent decades. 'Over-mobile', it travelled down 1.95 km, threatening a construction site. This multi-method study showed that the collapse occurred under conditions particularly favourable for the degradation of permafrost. Nevertheless, modelling of surface and temperatures at depth indicates positive temperatures. Although permafrost does not appear to be directly involved in triggering the collapse, the melting of ice lenses still present in the scar may have contributed to it, as may glacial retreat, which could be a major factor in triggering the rockfall (paraglacial rock slope instability). The significant amount of ice (~75%?) in the deposit indicates the intense erosion endured by the glacier and explains the complex gravity-driven mass flow. In the months following the main collapse, the scar remained particularly active, with a landslide of ~8000 m^3 accompanied by a series of rockfalls. The deposit experienced two distinct phases: a phase during which snow avalanches accumulated on the deposit and a torrential phase during which the rock deposit was gradually evacuated without debris flow. After the 2018 event, various measures have been taken to manage the risks associated with maintenance operations on a hydroelectric water intake.

The event can be seen as a new expression of cascading risks for valley floors. Is this the shape of things to come? The changing nature of risks in high mountain areas in the context of increasing vulnerability and warming climate (i) requires new approaches of integrated and collaborative management, (ii) shows the need for a holistic view (e.g., multi-hazard, cascading processes), (iii) demonstrates the importance of high-frequency data acquisition/analysis/interpretation and (iv) the need to manage uncertainty in glacial and torrential basins.

Author Contributions: Conceptualization, L.R., P.-A.D., L.A. and T.F.; methodology, L.R., P.-A.D., L.A., T.F., J.B., F.M. and A.B.; validation, L.R., P.-A.D., T.F. and P.D.; formal analysis, L.R., P.-A.D., L.A., T.F., J.B., M.C., F.M. and A.B.; investigation, L.R., P.-A.D., L.A., T.F., P.D., J.B., M.C., F.M. and A.B.; data curation, L.R., P.-A.D., L.A., T.F., P.D., J.B., M.C., F.M., A.B. and X.B.; writing—original draft preparation, L.R., P.-A.D., L.A., T.F., P.D., J.B., M.C., F.M., A.B., X.B. and P.D.; writing—review and editing, L.R., P.-A.D., L.A., T.F., P.D., J.B., M.C., F.M., A.B. and X.B.; supervision, L.R.; project administration, L.R.; funding acquisition, L.R., P.-A.D. and T.F. All authors have read and agreed to the published version of the manuscript.

Funding: This research was funded by the EU POIA *PermaRisk* project and the Direction Générale de la Prévention des Risques (DGPR) of the French Ministry in Charge of the Environment (MTECT).

Institutional Review Board Statement: Not applicable.

Informed Consent Statement: Not applicable.

Data Availability Statement: Data are available from the authors.

Acknowledgments: The authors thank *Voltalia* and the *Vallée de Chamonix Mont-Blanc* for facilitating this study. They would also like to thank Jean-Matthieu MONNET (INRAE), Emmanuel Malet (EDYTEM) and Éric Courcier for the use of the 2008 LiDAR digital terrain model, his help with the automatic photography, and the regular photographs of the scar, respectively.

Conflicts of Interest: The authors declare no conflict of interest.

References

1. Allen, S.; Huggel, C. Extremely warm temperatures as a potential cause of recent high mountain rockfall. *Glob. Planet. Chang.* **2013**, *107*, 59–69.
2. Bessette-Kirton, E.K.; Coe, J.A. A 36-year record of rock avalanches in the Saint Elias Mountains of Alaska, with implications for future hazards. *Front. Earth Sci.* **2020**, *8*, 293.
3. Ravanel, L.; Deline, P. Climate influence on rockfalls in high-Alpine steep rockwalls: The North side of the Aiguilles de Chamonix (Mont Blanc massif) since the end of the Little Ice Age. *Holocene* **2011**, *21*, 357–365.
4. Duvillard, P.-A.; Ravanel, L.; Marcer, M.; Schoeneich, P. Recent evolution of damage to infrastructure on permafrost in the French Alps. *Reg. Environ. Chang.* **2019**, *19*, 1281–1293.
5. Mergili, M.; Jaboyedoff, M.; Pullarello, J.; Pudasaini, S.P. Back calculation of the 2017 Piz Cengalo–Bondo landslide cascade with r.avaflow: What we can do and what we can learn. *Nat. Hazards Earth Syst. Sci.* **2020**, *20*, 505–520.
6. Barsch, D.; Caine, N. The nature of mountain geomorphology. *Mt. Res. Dev.* **1984**, *4*, 287–298. [CrossRef]
7. Haeberli, W. On the morphodynamics of iceldebris-transport systems in cold mountain areas. *Nor. J. Geogr.* **1996**, *50*, 3–9.
8. Kirschbaum, D.; Watson, C.S.; Rounce, D.R.; Shugar, D.H.; Kargel, J.S.; Haritashya, U.K.; Amatya, P.; Shean, D.; Anderson, E.R.; Jo, M. The state of remote sensing capabilities of cascading hazards over high mountain Asia. *Front. Earth Sci.* **2019**, *7*, 197.
9. Chen, N.; Liu, M.; Allen, S.; Deng, M.; Khanal, N.R.; Peng, T.; Tian, S.; Huggel, C.; Wu, K.; Rahman, M.; et al. Small outbursts into big disasters: Earthquakes exacerbate climate-driven cascade processes of the glacial lakes failure in the Himalayas. *Geomorphology* **2023**, *422*, 108539.
10. Deline, P.; Gardent, M.; Magnin, F.; Ravanel, L. The morphodynamics of the mont blanc massif in a changing cryosphere: A comprehensive review. *Geogr. Ann. Ser. A* **2012**, *94*, 265–283.
11. Messenzehl, K.; Meyer, H.; Otto, J.-C.; Hoffmann, T.; Dikau, R. Regional-scale controls on the spatial activity of rockfalls (Turtmann Valley, Swiss Alps)—A multivariate modeling approach. *Geomorphology* **2017**, *287*, 29–45. [CrossRef]
12. Knoflach, B.; Tussetschläger, H.; Sailer, R.; Meißl, G.; Stötter, J. High mountain rockfall dynamics: Rockfall activity and runout assessment under the aspect of a changing cryosphere. *Geogr. Ann. Ser. A* **2021**, *103*, 83–102. [CrossRef]
13. Walter, F.; Amann, F.; Kos, A.; Kenner, R.; Phillips, M.; de Preux, A.; Huss, M.; Tognacca, C.; Clinton, J.; Diehl, T.; et al. Direct observations of a three million cubic meter rock-slope collapse with almost immediate initiation of ensuing debris flows. *Geomorphology* **2020**, *351*, 106933. [CrossRef]
14. Ravanel, L.; Magnin, F.; Deline, P. Impacts of the 2003 and 2015 summer heat waves on permafrost-affected rockwalls in the Mont Blanc massif. *Sci. Total Environ.* **2017**, *609*, 132–143. [CrossRef] [PubMed]
15. Paranunzio, R.; Chiarle, M.; Laio, F.; Nigrelli, G.; Turconi, L.; Luino, F. New insights in the relation between climate and slope failures at high-elevation sites. *Theor. Appl. Climatol.* **2019**, *137*, 1765–1784. [CrossRef]
16. Fischer, L.; Amann, F.; Moore, J.R.; Huggel, C. Assessment of periglacial slope stability for the 1988 Tschierva rock avalanche (Piz Morteratsch, Switzerland). *Eng. Geol.* **2010**, *116*, 32–43. [CrossRef]
17. Phillips, M.; Wolter, A.; Lüthi, R.; Amann, F.; Kenner, R.; Bühler, Y. Rock slope failure in a recently deglaciated permafrost rock wall at Piz Kesch (Eastern Swiss Alps), February 2014. *Earth Surf. Process. Landf.* **2017**, *42*, 426–438. [CrossRef]
18. Deline, P. Interactions between rock avalanches and glaciers in the Mont Blanc massif during the late Holocene. *Quat. Sci. Rev.* **2009**, *28*, 1070–1083. [CrossRef]

19. Fei, L.; Jaboyedoff, M.; Guerin, A.; Noël, F.; Bertolo, D.; Derron, M.-H.; Thuegaz, P.; Troilo, F.; Ravanel, L. Assessing the rock failure return period on an unstable Alpine rock wall based on volume-frequency relationships: The Brenva Spur (3916 m a.s.l., Aosta Valley, Italy). *Eng. Geol.* **2023**, *323*, 107239. [CrossRef]
20. Wichmann, V.; Heckmann, T.; Haas, F.; Becht, M. A new modelling approach to delineate the spatial extent of alpine sediment cascades. *Geomorphology* **2009**, *111*, 70–78. [CrossRef]
21. Pigeon, P. Représentation cartographique du risque et vulnérabilité liée à la pression foncière touristique (Taconnaz, Les Houches et Vers-le-Nant, Chamonix). *Rev. De Géogr. Alp.* **1998**, *86*, 101–113. [CrossRef]
22. Naaim, M.; Faug, T.; Naaim, F.; Eckert, N. Return period calculation and passive structure design at the Taconnaz avalanche path, France. *Ann. Glaciol.* **2010**, *51*, 89–97. [CrossRef]
23. Vincent, C.; Thibert, E.; Harter, M.; Soruco, A.; Gilbert, A. Volume and frequency of ice avalanches from Taconnaz hanging glacier, French Alps. *Ann. Glaciol.* **2015**, *56*, 17–25. [CrossRef]
24. Gilbert, A.; Vincent, C.; Gagliardini, O.; Krug, J.; Berthier, E. Assessment of thermal change in cold avalanching glaciers in relation to climate warming. *Geophys. Res. Lett.* **2015**, *42*, 6382–6390. [CrossRef]
25. Guerin, A.; Abellán, A.; Matasci, B.; Jaboyedoff, M.; Derron, M.-H.; Ravanel, L. 3D reconstruction of a collapsed rock pillar from web-retrieved images and terrestrial LiDAR data—The 2005 event of the West face of the Drus (Mont-Blanc massif). *Nat. Hazards Earth Syst. Sci.* **2017**, *17*, 1207–1220. [CrossRef]
26. Deline, P.; Kirkbride, M.P.; Ravanel, L.; Ravello, M. The Tré-la-Tête rockfall onto the glacier de la Lex Blanche (Mont Blanc massif, Italy) in September 2008. *Geogr. Fis. E Din. Quat.* **2008**, *31*, 251–254.
27. Ravanel, L.; Deline, P. A network of observers in the Mont Blanc massif to study rockfalls from high alpine rockwalls. *Geogr. Fis. E Din. Quat.* **2013**, *36*, 151–158.
28. Deline, P.; Alberto, W.; Broccolato, M.; Hungr, O.; Noetzli, J.; Ravanel, L.; Tamburini, A. The December 2008 Crammont rock avalanche, Mont Blanc massif area, Italy. *Nat. Hazards Earth Syst. Sci.* **2011**, *11*, 3307–3318. [CrossRef]
29. Randolph Glacier Inventory (RGI Consortium). *A Dataset of Global Glacier Outlines: Version 6.0*; Technical Report, Global Land Ice Measurements from Space; National Snow and Ice Data Center (NSIDC): Boulder, CO, USA, 2017. [CrossRef]
30. Zemp, M.; Huss, M.; Thibert, E.; Eckert, N.; McNabb, R.; Huber, J.; Barandun, M.; Machguth, H.; Nussbaumer, S.U.; Gärtner-Roer, I.; et al. Global glacier mass changes and their contributions to sea-level rise from 1961 to 2016. *Nature* **2019**, *568*, 382–386. [CrossRef]
31. Gardent, M.; Rabatel, A.; Dedieu, J.-P.; Deline, P. Multitemporal glacier inventory of the French Alps from the late 1960s to the late 2000s. *Glob. Planet. Chang.* **2014**, *120*, 24–37. [CrossRef]
32. Huss, M. Extrapolating glacier mass balance to the mountain-range scale: The European Alps 1900–2100. *Cryosphere* **2012**, *6*, 713–727. [CrossRef]
33. Zemp, M.; Frey, H.; Gärtner-Roer, I.; Nussbaumer, S.U.; Hoelzle, M.; Paul, F.; Haeberli, W.; Denzinger, F.; Ahlstroem, A.P.; Anderson, B.; et al. Historically unprecedented global glacier decline in the early 21st century. *J. Glaciol.* **2015**, *61*, 745–762. [CrossRef]
34. Davaze, L.; Rabatel, A.; Dufour, A.; Hugonnet, R.; Arnaud, Y. Region-wide annual glacier surface mass balance for the European Alps from 2000 to 2016. *Front. Earth Sci.* **2020**, *8*, 149. [CrossRef]
35. Deline, P.; Gruber, S.; Amann, F.; Bodin, X.; Delaloye, R.; Failletaz, J.; Fischer, L.; Geertsema, M.; Giardino, M.; Hasler, A.; et al. Ice loss from glaciers and permafrost and related slope instability in high-mountain regions. In *Snow and Ice-Related Hazards, Risks, and Disasters*, 2nd ed.; Haeberli, W., Whiteman, C., Eds.; Hazards and Disasters Series; Elsevier: Amsterdam, The Netherlands, 2021; pp. 501–540.
36. Failletaz, J.; Sornette, D.; Funk, M. Instabilities on Alpine temperate glaciers: New insights arising from the numerical modelling of Allalingletscher (Valais, Switzerland). *Nat. Hazards Earth Syst. Sci.* **2012**, *12*, 2977–2991. [CrossRef]
37. Giordan, D.; Dematteis, N.; Allasia, P.; Motta, E. Classification and kinematics of the Planpincieux Glacier breakoffs using photographic time-lapse analysis. *J. Glaciol.* **2020**, *66*, 188–202. [CrossRef]
38. Faillettaz, J.; Funk, M.; Vincent, C. Avalanching glacier instabilities: Review on processes and early warning perspectives. *Rev. Geophys.* **2015**, *53*, 203–224. [CrossRef]
39. Gilbert, A.; Vincent, C. Atmospheric temperature changes over the 20th century at very high elevations in the European Alps from englacial temperatures. *Geophys. Res. Lett.* **2013**, *40*, 2102–2108. [CrossRef]
40. Mortara, G.; Tamburini, A. *Il Ghiacciao del Belvedere e l'emergenza del lago Effimero*; Società Meteorologica Subalpina: Bussoleno, Italy, 2009; 192p.
41. Worni, R.; Stoffel, M.; Huggel, C.; Volz, C.; Casteller, A.; Luckman, B.H. Analysis and dynamic modeling of a moraine failure and glacier lake outburst flood at Ventisquero Negro, Patagonian Andes (Argentina). *J. Hydrol.* **2012**, *444–445*, 134–145. [CrossRef]
42. Duvillard, P.-A.; Ravanel, L.; Deline, P.; Dubois, L. Paraglacial rock slope adjustment below a high mountain infrastructure: The Pilatte hut case study (Écrins moutain range, France). *Front. Earth Sci.* **2018**, *6*, 94. [CrossRef]
43. Ravanel, L.; Duvillard, P.-A.; Jaboyedoff, M.; Lambiel, C. Recent evolution of an ice-cored moraine at the Gentianes Pass, Valais Alps, Switzerland. *Land Degrad. Dev.* **2018**, *29*, 3693–3708. [CrossRef]
44. Biskaborn, B.K.; Smith, S.L.; Noetzli, J.; Matthes, H.; Vieira, G.; Streletskiy, D.A.; Schoeneich, P.; Romanovsky, V.E.; Lewkowicz, A.G.; Abramov, A.; et al. Permafrost is warming at a global scale. *Nat. Commun.* **2019**, *10*, 264. [CrossRef]

45. Etzelmüller, B.; Guglielmin, M.; Hauck, C.; Hilbich, C.; Hoelzle, M.; Isaksen, K.; Noetzli, J.; Oliva, M.; Ramos, M. Twenty years of European mountain permafrost dynamics—The PACE legacy. *Environ. Res. Lett.* **2020**, *15*, 104070. [CrossRef]
46. Gruber, S.; Haeberli, W. Permafrost in steep bedrock slopes and its temperature-related destabilization following climate change. *J. Geophys. Res.* **2007**, *112*, F00547. [CrossRef]
47. Viani, C.; Machguth, H.; Huggel, C.; Godio, A.; Franco, D.; Perotti, L.; Giardino, M. Potential future lakes from continued glacier shrinkage in the Aosta Valley Region (Western Alps, Italy). *Geomorphology* **2020**, *355*, 107068. [CrossRef]
48. Huggel, C.; Kääb, A.; Haeberli, W.; Krummenacher, B. Regional-scale GIS-models for assessment of hazards from glacier lake outbursts: Evaluation and application in the Swiss Alps. *Nat. Hazards Earth Syst. Sci.* **2003**, *3*, 647–662. [CrossRef]
49. Chiarle, M.; Iannotti, S.; Mortara, G.; Deline, P. Recent debris flow occurrences associated with glaciers in the Alps. *Glob. Planet. Chang.* **2007**, *56*, 123–136. [CrossRef]
50. Krautblatter, M.; Verleysdonk, S.; Flores-Orozco, A.; Kemna, A. Temperature-calibrated imaging of seasonal changes in permafrost rock walls by quantitative electrical resistivity tomog-raphy (Zugspitze, German/Austrian Alps). *J. Geophys. Res.* **2010**, *115*, F02003.
51. Krautblatter, M.; Funk, D.; Günzel, F.K. Why permafrost rocks become unstable: A rock ice-mechanical model in time and space. *Earth Surf. Process. Landf.* **2013**, *38*, 876–887. [CrossRef]
52. Draebing, D.; Krautblatter, M. P-wave velocity changes in freezing hard low-porosity rocks: A laboratory-based time-average model. *Cryosphere* **2012**, *6*, 1163–1174. [CrossRef]
53. Noetzli, J.; Gruber, S. Transient thermal effects in Alpine permafrost. *Cryosphere* **2009**, *3*, 85–99. [CrossRef]
54. Hasler, A.; Gruber, S.; Font, M.; Dubois, A. Advective heat transport in frozen rock clefts: Conceptual model, laboratory experiments and numerical simulation. *Permafr. Periglac. Process.* **2011**, *22*, 378–389. [CrossRef]
55. Draebing, D.; Krautblatter, M.; Dikau, R. Interaction of thermal and mechanical processes in steep permafrost rock walls: A conceptual approach. *Geomorphology* **2014**, *226*, 226–235. [CrossRef]
56. Cicoira, A.; Marcer, M.; Gärtner-Roer, I.; Bodin, X.; Arenson, L.U.; Vieli, A. A general theory of rock glacier creep based on *in-situ* and remote sensing observations. *Permafr. Periglac. Process.* **2021**, *32*, 139–153. [CrossRef]
57. Pellet, C.; Bodin, X.; Delaloye, R.; Kaufmann, V.; Noetzli, J.; Thibert, E.; Kellerer-Pirklbauer, A. Rock glacier kinematics. *Bull. Am. Meteorol. Soc.* **2021**, *102*, S44–S45.
58. Kenner, R.; Pruessner, L.; Beutel, J.; Limpach, P.; Phillips, M. How rock glacier hydrology, deformation velocities and ground temperatures interact: Examples from the Swiss Alps. *Permafr. Periglac. Process.* **2019**, *31*, 3–14. [CrossRef]
59. Marcer, M.; Cicoira, A.; Cusicanqui, D.; Bodin, X.; Echelard, T.; Obregon, R.; Schoeneich, P. Rock glaciers throughout the French Alps accelerated and destabilised since 1990 as air temperatures increased. *Nat. Commun. Earth Environ.* **2021**, *2*, 81. [CrossRef]
60. O'Connor, J.E.; Costa, J.E. Geologic and hydrologic hazards in glacierized basins in North America resulting from 19th and 20th century global warming. *Nat. Hazards* **1993**, *8*, 121–140. [CrossRef]
61. Haeberli, W.; Burn, C.R. Natural hazards in forests: Glacier and permafrost effects as related to climate change. In *Environmental Change and Geomorphic Hazards in Forests*; Sidle, R.C., Ed.; CABI Publishing: Wallingford, UK, 2002; pp. 167–202.
62. Watson, R.T.; Haeberli, W. Environmental threats, mitigation strategies and high-hountain areas. *AMBIO J. Hum. Environ.* **2004**, *13*, 2–10. [CrossRef]
63. Kääb, A.; Reynolds, J.M.; Haeberli, W. Glacier and permafrost hazards in high mountains. In *Global Change and Mountain Regions*; Huber, U.M., Bugmann, H.K.M., Reasoner, M.A., Eds.; Springer: Dordrecht, The Netherlands, 2005; pp. 225–234.
64. Moore, R.D.; Fleming, S.W.; Menounos, B.; Wheate, R.; Fountain, A.; Stahl, K.; Holm, K.; Jakob, M. Glacier change in western North America: Influences on hydrology, geomorphic hazards and water quality. *Hydrol. Process.* **2009**, *23*, 42–61. [CrossRef]
65. Clague, J.J. Climate change and slope instability. In *Landslides—Disaster Risk Reduction*; Sassa, K., Canuti, P., Eds.; Springer: Berlin/Heidelberg, Germany, 2009; pp. 557–572.
66. Kääb, A. Natural hazards associated with glaciers and permafrost. In *Encyclopedia of Snow, Ice and Glaciers*; Singh, V.P., Singh, P., Haritashya, U.K., Eds.; Springer: Berlin/Heidelberg, Germany, 2011; pp. 763–774.
67. Knight, J.; Harrison, S. Mountain glacial and paraglacial environments under global climate change: Lessons from the past, future directions and policy implications. *Geogr. Ann. Ser. A Phys. Geogr.* **2014**, *96*, 245–264. [CrossRef]
68. Church, M.; Ryder, J.M. Paraglacial sedimentation: A consideration of fluvial processes conditioned by glaciation. *Geol. Soc. Am. Bull.* **1972**, *83*, 3059–3072. [CrossRef]
69. Vilímek, V.; Emmer, A.; Huggel, C.; Schaub, Y.; Würmli, S. Database of glacial lake outburst floods (GLOFs)–IPL project No. 179. *Landslides* **2014**, *11*, 161–165. [CrossRef]
70. Ballantyne, C.K. Paraglacial geomorphology. *Quat. Sci. Rev.* **2002**, *21*, 1935–2017.
71. Schrott, L.; Götz, J.; Geilhausen, M.; Morche, D. Spatial and temporal variability of sediment transfer and storage in an Alpine basin (Reintal valley, Bavarian Alps, Gemany). *Geogr. Helv.* **2006**, *61*, 191–200. [CrossRef]
72. Berthet, J. L'évolution Géomorphologique des Systèmes Torrentiels Proglaciaires de la vallée de Chamonix-Mont-Blanc, une Approche du Couplage Sédimentaire de la fin du Petit Age Glaciaire au Désenglacement Récent. Ph.D. Thesis, Université Savoie Mont Blanc, Chambéry, France, 2016; 304p.
73. Bertini, G.; Marcucci, M.; Nevini, R.; Passerini, P.; Sguazzoni, G. Patterns of faulting in the Mont Blanc granite. *Tectonophysics* **1985**, *111*, 65–106. [CrossRef]

74. Leloup, P.H.; Arnaud, N.; Sobel, E.R.; Lacassin, R. Alpine thermal and structural evolution of the highest external crystalline massif: The Mont Blanc. *Tectonics* **2005**, *24*, TC4002. [CrossRef]
75. Boeckli, L.; Brenning, A.; Gruber, S.; Noetzli, J. Permafrost distribution in the European Alps: Calculation and evaluation of an index map and summary statistics. *Cryosphere* **2011**, *6*, 807–820. [CrossRef]
76. Magnin, F.; Brenning, A.; Bodin, X.; Deline, P.; Ravanel, L. Statistical modelling of rock wall permafrost distribution: Application to the Mont Blanc massif. *Géomorphologie* **2015**, *21*, 145–162. [CrossRef]
77. Vivian, R. *Des Glacières du Faucigny aux Glaciers du Mont-Blanc*; Collection Les Savoisiennes; La Fontaine de Siloé: Montmélian, France, 2001; 296p.
78. Mougin, P. *Les Torrents de la Savoie*; Société d'Histoire Naturelle de Savoie; Grands Etablissements de l'Imprimerie Générale: Grenoble, France, 1914; 1251p.
79. Le Meur, E.; Vincent, C. Monitoring of the Taconnaz ice fall (French Alps) using measurements of mass balance, surface velocities and ice cliff position. *Cold Reg. Sci. Technol.* **2006**, *46*, 1–11. [CrossRef]
80. Vincent, C.; Gilbert, A.; Piard, L.; Gagliardini, O.; Jourdain, B.; Gimbert, F.; Christoffersen, P. *Englacial Temperatures Increase of Taconnaz Glacier (Mont Blanc Area) and Consequences on Glacier Instability in the Future*; EGU22-4778; EGU General Assembly 2022: Vienna, Austria, 2022.
81. Berthet-Rambaud, P.; Limam, A.; Roenelle, P.; Rapin, F.; Tacnet, J.-M.; Mazars, J. Avalanche action on rigid structures: Back-analysis of Taconnaz deflective walls' collapse in February 1999. *Cold Reg. Sci. Technol.* **2007**, *47*, 16–31. [CrossRef]
82. Bellot, H.; Naaim-Bouvet, F.; Naaim, M.; Caccamo, P.; Faug, T.; Ousset, F. Taconnaz avalanche path: Pressure and velocity. In Proceedings of the International Snow Science Workshop (ISSW 2013), Grenoble Chamonix-Mont-Blanc, France, 7–11 October 2013; pp. 1378–1388.
83. Naaim, M.; Faug, T.; Naaim-Bouvet, F.; Eckert, N. Effectiveness of avalanche protection structures in run-out zones: The Taconnaz avalanche path case in France. In *Proceedings of the International Snow Science Workshop, Innsbruck, Austria, 7–12 October 2018*; 5p.
84. Hsü, K.J. Catastrophic debris streams (sturzstroms) generated by rockfalls. *Geol. Soc. Am. Bull.* **1975**, *86*, 129–140.
85. Evans, S.G.; Clague, J.J. Recent climatic change and catastrophic geomorphic processes in mountain environments. *Geomorphology* **1994**, *10*, 107–128.
86. Geertsema, M.; Clague, J.J.; Schwab, J.W.; Evans, S.G. An overview of recent large catastrophic landslides in Northern British Columbia, Canada. *Eng. Geol.* **2006**, *83*, 120–143.
87. Okura, Y.; Kitahara, H.; Sammori, T.; Kawanami, A. The effects of rockfall volume on runout distance. *Eng. Geol.* **2000**, *58*, 109–124.
88. Rabatel, A.; Deline, P.; Jaillet, S.; Ravanel, L. Rock falls in high-alpine rock walls quantified by terrestrial lidar measurements: A case study in the Mont Blanc area. *Geophys. Res. Lett.* **2008**, *35*, L10502.
89. Heckmann, T.; Bimböse, M.; Krautblatter, M.; Haas, F.; Becht, M.; Morche, D. From geotechnical analysis to quantification and modelling using LiDAR data: A study on rockfall in the Reintal catchment, Bavarian Alps, Germany. *Earth Surf. Process. Landf.* **2012**, *37*, 119–133.
90. Hendrickx, H.; Le Roy, G.; Helmstetter, A.; Pointner, E.; Larose, E.; Braillard, L.; Nyssen, J.; Delaloye, R.; Frankl, A. Timing, volume and precursory indicators of rock- and cliff fall on a permafrost mountain ridge (Mattertal, Switzerland). *Earth Surf. Process. Landf.* **2022**, *47*, 1532–1549.
91. Jaboyedoff, M.; Oppikofer, T.; Abellán, A.; Derron, M.-H.; Loye, A.; Metzger, R.; Pedrazzini, A. Use of LIDAR in landslide investigations: A review. *Nat. Hazards* **2012**, *61*, 5–28.
92. Buill, F.; Núñez-Andrés, M.A.; Lantada, N.; Prades, A. Comparison of photogrammetric techniques for rockfalls monitoring. *IOP Conf. Ser. Earth Environ. Sci.* **2016**, *44*, 042023.
93. Westoby, M.; Lim, M.; Hogg, M.; Dunlop, L.; Pound, M.; Strzelecki, M.; Woodward, J. Decoding complex erosion responses for the mitigation of coastal rockfall hazards using repeat terrestrial LiDAR. *Remote Sens.* **2020**, *12*, 2620.
94. DiFrancesco, P.-M.; Bonneau, D.A.; Hutchinson, D.J. Computational geometry-based surface reconstruction for volume estimation: A case study on magnitude-frequency relations for a LiDAR-derived rockfall inventory. *ISPRS Int. J. Geo-Inf.* **2021**, *10*, 157.
95. Graber, A.; Santi, P. UAV-photogrammetry rockfall monitoring of natural slopes in Glenwood Canyon, CO, USA: Background activity and post-wildfire impacts. *Landslides* **2023**, *20*, 229–248.
96. Guerin, A.; Ravanel, L.; Matasci, B.; Jaboyedoff, M.; Deline, P. The three-stage rock failure dynamics of the Drus (Mont Blanc massif, France) since the June 2005 large event. *Nat. Sci. Rep.* **2020**, *10*, 17330.
97. Smith, M.W.; Carrivick, J.L.; Quincey, D.J. Structure from motion photogrammetry in physical geography. *Prog. Phys. Geogr. Earth Environ.* **2016**, *40*, 247–275.
98. Naaim, M.; Naaim-Bouvet, F.; Faug, T.; Bouchet, A. Dense snow avalanche modeling: Flow, erosion, deposition and obstacle effects. *Cold Reg. Sci. Technol.* **2004**, *39*, 193–204.
99. Voellmy, A. Über die Zerstörungskraft von Lawinen. *Schweiz. Bauztg. Jahrg* **1955**, *73*, 12, 159–162, 212–217, 246–249 and 280–285.
100. Pirulli, M.; Mangeney, A. Results of back-analysis of the propagation of rock avalanches as a function of the assumed rheology. *Rock Mech. Rock Eng.* **2008**, *41*, 59–84.
101. Margreth, S.; Failletaz, J.; Funk, M.; Vagliasindi, M.; Diotri, F.; Broccolato, M. Safety concept for hazards caused by ice avalanches from the Whymper hanging glacier in the Mont Blanc Massif. *Cold Reg. Sci. Technol.* **2011**, *69*, 194–201.

102. Kääb, A.; Leinss, S.; Gilbert, A.; Bühler, Y.; Gascoin, S.; Evans, S.G.; Bartelt, P.; Berthier, E.; Brun, F.; Chao, W.-A.; et al. Massive collapse of two glaciers in western Tibet in 2016 after surge-like instability. *Nat. Geosci.* **2018**, *11*, 114–120.
103. Thibert, E.; Faug, T.; Gilbert, A.; Vincent, C.; Gagliardini, O.; Naaim, M.; Bonnefoy-Demongeot, M.; Funk, M. Retrieving Ice-avalanche basal friction law parameters from a back-analysis of the collapse of Altels glacier (1895, Bernese Alps, Switzerland). Application to Taconnaz glacier instability (French Alps). In Proceedings of the International Snow Science Workshop, Innsbruck, Austria, 7–12 October 2018; pp. 66–70.
104. Frank, F.; Huggel, C.; McArdell, B.W.; Vieli, A. Landslides and increased debris-flow activity: A systematic comparison of six catchments in Switzerland. *Earth Surf. Process. Landf.* **2019**, *44*, 699–712.
105. Huggel, C. Recent extreme slope failures in glacial environments: Effects of thermal perturbation. *Quat. Sci. Rev.* **2009**, *28*, 1119–1130.
106. Gruber, S.; Hoelzle, M.; Haeberli, W. Permafrost thaw and destabilization of Alpine rock walls in the hot summer of 2003. *Geophys. Res. Lett.* **2004**, *31*, L13504. [CrossRef]
107. Legay, A.; Magnin, F.; Ravanel, L. Rock temperature prior to failure: Analysis of 209 rockfall events in the Mont Blanc massif (Western European Alps). *Permafr. Periglac. Process.* **2021**, *32*, 520–536. [CrossRef]
108. Magnin, F.; Deline, P.; Ravanel, L.; Noetzli, J.; Pogliotti, P. Thermal characteristics of permafrost in the steep alpine rock walls of the Aiguille du Midi (Mont Blanc Massif, 3842 m a.s.l.). *Cryosphere* **2015**, *9*, 109–121. [CrossRef]
109. McColl, S.T. Paraglacial rock-slope stability. *Geomorphology* **2012**, *153–154*, 1–16.
110. Wieczorek, G.F.; Jäger, S. Triggering mechanisms and depositional rates of postglacial slope-movement processes in the Yosemite Valley, California. *Geomorphology* **1996**, *15*, 17–31. [CrossRef]
111. Cossart, E.; Braucher, R.; Fort, M.; Bourlès, D.L.; Carcaillet, J. Slope instability in relation to glacial debuttressing in alpine areas (Upper Durance catchment, southeastern France): Evidence from field data and ^{10}Be cosmic ray exposure ages. *Geomorphology* **2008**, *95*, 3–26.
112. McColl, S.T.; Davies, T.R.H. Large ice-contact slope movements: Glacial buttressing, deformation and erosion. *Earth Surf. Process. Landf.* **2013**, *38*, 1102–1115.
113. Kos, A.; Amann, F.; Strozzi, T.; Delaloye, R.; von Ruette, J.; Springman, S. Contemporary glacier retreat triggers a rapid landslide response, Great Aletsch Glacier, Switzerland. *Geophys. Res. Lett.* **2016**, *43*, 071708.
114. Grämiger, L.M.; Moore, J.R.; Gischig, V.S.; Ivy-Ochs, S.; Loew, S. Beyond debuttressing: Mechanics of paraglacial rock slope damage during repeat glacial cycles. *J. Geophys. Res. Earth Surf.* **2017**, *122*, 1004–1036.
115. Zanoner, T.; Carton, A.; Seppi, R.; Carturan, L.; Baroni, C.; Salvatore, M.C.; Zumiani, M. Little Ice Age mapping as a tool for identifying hazard in the paraglacial environment: The case study of Trentino (Eastern Italian Alps). *Geomorphology* **2017**, *295*, 551–562. [CrossRef]
116. Oppikofer, T.; Jaboyedoff, M.; Blikra, L.; Derron, M.-H.; Metzger, R. Characterization and monitoring of the Åknes rockslide using terrestrial laser scanning. *Nat. Hazards Earth Syst. Sci.* **2009**, *9*, 1003–1019. [CrossRef]
117. Blair, R.W. Moraine and valley wall collapse due to rapid deglaciation in Mount Cook National Park, New Zealand. *Mt. Res. Dev.* **1994**, *14*, 347–358. [CrossRef]
118. Li, D.; Lu, X.; Walling, D.E.; Zhang, T.; Steiner, J.F.; Wasson, R.J.; Harrison, S.; Nepal, S.; Nie, Y.; Immerzeel, W.W.; et al. High Mountain Asia hydropower systems threatened by climate-driven landscape instability. *Nat. Geosci.* **2022**, *15*, 520–530. [CrossRef]
119. Yu, G.-A.; Yao, W.; Huang, H.Q.; Liu, Z. Debris flows originating in the mountain cryosphere under a changing climate: A review. *Prog. Phys. Geogr. Earth Environ.* **2021**, *45*, 339–374. [CrossRef]
120. Carrivick, J.L.; Tweed, F.S. A global assessment of the societal impacts of glacier outburst floods. *Glob. Planet. Chang.* **2016**, *144*, 1–16. [CrossRef]
121. Meier, L.; Jacquemart, M.; Steinacher, R.; Jäger, D.; Funk, M. Monitoring of the Weissmies glacier before the failure event of September 10, 2017 with radar interferometry and high-resolution deformation came. In Proceedings of the International Snow Science Workshop, Innsbruck, Austria, 7–12 October 2018; pp. 661–664.
122. Marsy, G.; Vernier, F.; Trouvé, E.; Bodin, X.; Castaings, W.; Walpersdorf, A.; Malet, E.; Girard, B. Temporal consolidation strategy for ground-based image displacement time series: Application to glacier monitoring. *IEEE J. Sel. Top. Appl. Earth Obs. Remote Sens.* **2021**, *14*, 10069–10078. [CrossRef]
123. Dematteis, N.; Giordan, D.; Troilo, F.; Wrzesniak, A.; Godone, D. Ten-year monitoring of the Grandes Jorasses glaciers kinematics. Limits, potentialities, and possible applications of different monitoring systems. *Remote Sens.* **2021**, *13*, 3005. [CrossRef]
124. Egli, P.E.; Belotti, B.; Ouvry, B.; Irving, J.; Lane, S.N. Subglacial channels, climate warming, and increasing frequency of Alpine glacier snout collapse. *Geophys. Res. Lett.* **2021**, *48*, e2021GL096031. [CrossRef]
125. Jourdan-Laforte, M. La débâcle glaciaire de la Mer de Glace. *Rev. Géogr. Alp.* **1920**, *8*, 535–539. [CrossRef]
126. Zheng, G.; Mergili, M.; Emmer, A.; Allen, S.; Bao, A.; Guo, H.; Stoffel, M. The 2020 glacial lake outburst flood at Jinwuco, Tibet: Causes, impacts, and implications for hazard and risk assessment. *Cryosphere* **2021**, *15*, 3159–3180. [CrossRef]
127. Mourey, J.; Lacroix, P.; Duvillard, P.-A.; Marsy, G.; Marcer, M.; Malet, E.; Ravanel, L. Multi-method monitoring of rockfall activity along the classic route up Mont Blanc (4809 m a.s.l.) to encourage adaptation by mountaineers. *Nat. Hazards Earth Syst. Sci.* **2022**, *22*, 445–460. [CrossRef]